Lai et al. *Zool. Res.* 2026, 47(6): 1980−2002
https://doi.org/10.24272/j.issn.2095-8137.2025.623
https://cstr.cn/32248.14.zr.2025.623

ZR | Zoological Research

Article Open Access

Single-cell profiling of cross-tissue features of fetal pig macrophages and their remodeling in fetal growth restriction

Chen-Liang Lai[1,#], Xiao-Yun Chen[1,#], Li-Ping Cai[1,*]

[1] *National Key Laboratory for Swine Genetic Improvement and Germplasm Innovation*, *Ministry of Science and Technology of China*, *Jiangxi Agricultural University*, *Nanchang*, *Jiangxi* 330045, *China*

ABSTRACT

Macrophages are highly heterogeneous immune cells with context-dependent functions, yet their diversity across prenatal tissues of the whole body, sexes, and stages remains elusive. During fetal development, macrophages play essential roles in tissue formation and maintaining maternal-fetal immune balance, but their specific phenotypic and functional changes in the context of fetal growth restriction remain relatively underexplored. Herein, we constructed a cross-tissue macrophage atlas of 85 473 cells from 54 tissues of late-gestation fetal pigs. We identified 15 macrophage subtypes, among which two Hofbauer cell (HBC) subtypes were distinguished by their distinct transcriptional and functional characteristics between the amniotic and chorioallantoic membranes: HBC GPNMB+ cells upregulated glycolytic enzymes and extracellular matrix regulators such as *LDHA* and *GPNMB*, while HBC PEG10+ cells expressed immunomodulators and developmental regulators, including *A2M* and *PEG10*. Two dichotomous subtypes, LYVE1^{high}MHCII^{low} and LYVE1^{low}MHCII^{high}, were delineated across 27 tissues, with a conserved transcriptional signature in pigs and humans. Transcriptional profiling of metabolic pathways revealed oxidative phosphorylation and the tricarboxylic acid cycle as core pathways across tissues, alongside tissue-specific adaptations such as enhanced glycolysis in amniotic macrophages. Cross-stage comparisons showed fetal macrophages mainly maintained developmental programs, whereas adult macrophages globally exhibited heightened immune activity. Cross-sex and cross-species analyses revealed high transcriptomic similarity in fetal macrophages. In growth-restricted fetuses, chorioallantoic HBCs showed profound remodeling, including increased inflammation, hypoxia response, and vascular dysfunction signaling, with altered intercellular communication. Collectively, this work provides a comprehensive resource for understanding fetal macrophage heterogeneity and offers insights into the potential mechanisms underlying fetal growth restriction.

Keywords: Fetal pigs; Macrophages; Single-cell RNA sequencing; Cross-tissue; Fetal growth restriction

INTRODUCTION

Tissue-resident macrophages (TRMs) originate during embryonic development, where they are seeded into developing tissues through successive waves of hematopoiesis (Ginhoux & Guilliams, 2016). They undergo further specialization under the combined influence of lineage-determining transcription factors (TFs) and local niche signals, giving rise to tissue-specific subtypes that persist after birth (Lazarov et al., 2023; Mass et al., 2016). These TRMs exhibit remarkable functional diversity, contributing to immune defense, tissue remodeling, and homeostasis, with their phenotypes finely tuned to the requirements of distinct tissue environments (Guan et al., 2025). Central to this plasticity are TFs, which serve as master regulators of macrophage development, lineage commitment, survival, and functional specialization by integrating intrinsic lineage programs with extrinsic environmental cues (Lazarov et al., 2023). Classic examples include *SALL1*, which specifies the identity of brain microglia (MG) responsible for synaptic pruning (Holtman et al., 2017; Li & Barres, 2018); *ID3*, which determines the fate of liver Kupffer cells (KCs) involved in iron recycling (Deng et al., 2024; Jenne & Kubes, 2013); and *SPIC*, a fate-determining factor for splenic red pulp macrophages (RPMs) that coordinate erythrocyte turnover (Lavin et al., 2015; Xu & Huang, 2020). Fetal and adult macrophages share a conserved core of TFs such as *Maf*, *Batf3*, *Pparg*, *Irf8*, and *Zeb2* (Mass et al., 2016), yet also display developmental stage-specific expression programs. For example, Frenis et al. (2025) demonstrated that fetal macrophages show higher expression of *HES1* and *MYC* compared to adult macrophages. During fetal development, the fetus resides in a rapidly changing environment shaped by organogenesis,

This is an open-access article distributed under the terms of the Creative Commons Attribution Non-Commercial License (http://creativecommons.org/licenses/by-nc/4.0/), which permits unrestricted non-commercial use, distribution, and reproduction in any medium, provided the original work is properly cited.

Copyright ©2026 Editorial Office of Zoological Research, Kunming Institute of Zoology, Chinese Academy of Sciences

Received: 13 March 2026; Accepted: 20 April 2026; Online: 21 April 2026

Foundation items: This study was supported by the National Natural Science Foundation of China (32402738)

[#]Authors contributed equally to this work

*Corresponding author, E-mail: Lipingcai93@hotmail.com

maternal–fetal metabolic exchange, and the unique requirement for immune tolerance at the maternal–fetal interface (Ander et al., 2019; Prabhudas et al., 2015). These developmental contexts necessitate both conserved transcriptional programs essential for macrophage identity and stage- or tissue-specific regulators that tailor their functions throughout ontogeny. Despite their fundamental importance, the transcriptional and functional heterogeneity of fetal macrophages across diverse tissues during late gestation remains poorly characterized.

Macrophage function is increasingly recognized to be tightly linked to cellular metabolism, which not only supplies energy and biosynthetic intermediates but also instructs activation states, effector programs, and tissue-specific functions (Davies et al., 2017; Nobs & Kopf, 2021; Wculek et al., 2024). Traditionally, macrophage metabolism has been conceptualized primarily through in vitro models, where pro-inflammatory (M1-like) macrophages preferentially rely on glycolysis and inducible nitric oxide synthase (iNOS) pathways to support antimicrobial and inflammatory responses (Wculek et al., 2022). In contrast, alternatively activated (M2-like) macrophages engage oxidative phosphorylation (OXPHOS), fatty acid oxidation (FAO), and glutaminolysis to sustain anti-inflammatory and tissue-remodeling programs (Wculek et al., 2022). However, these simplified models fail to capture in vivo complexity. Metabolic flow and mass cytometry, along with single-cell transcriptomics-based metabolic inference, have facilitated single-cell immunometabolism (Ahl et al., 2020; Artyomov & Van Den Bossche, 2020; Hartmann et al., 2021; Li et al., 2022), revealing remarkable metabolic plasticity of TRMs across tissues, which in turn shapes tissue-specific functions such as lipid handling, iron recycling, and phagocytosis (Davies et al., 2017; Heieis et al., 2023; Remmerie & Scott, 2018; Wculek et al., 2022, 2023). Despite these insights, the metabolic states of fetal macrophages across multiple tissues and their relationship to functional specialization during late gestation remain largely unexplored.

Single-cell transcriptomic technologies have greatly advanced our understanding of macrophage biology, uncovering heterogeneous compositions and specialized subsets distinguished by their developmental origins (Wang et al., 2023), anatomical niches (Domanska et al., 2022), and functional roles (Miyamoto et al., 2024). These studies, spanning both individual tissue and single-tissue comparisons, have consistently identified macrophage populations that reflect a balance between conserved core programs and tissue-specific adaptations (Chakarov et al., 2019; Dick et al., 2022; Wang et al., 2023). Among these diverse populations, the LYVE1^{high}MHCII^{low} and LYVE1^{low}MHCII^{high} subtypes stand out as species- and tissue-conserved subtypes, whose presence has been consistently observed in humans (Eraslan et al., 2022), mice (Chakarov et al., 2019; Lund et al., 2024), and zebrafish (Zhou et al., 2023a). LYVE1^{high}MHCII^{low} macrophages are generally associated with perivascular niches and vascular homeostasis, whereas LYVE1^{low}MHCII^{high} macrophages are more tightly linked to immune surveillance and antigen presentation. However, whether these conserved subtypes are similarly established in large mammals such as pigs and the extent to which they share similar transcriptional and functional features remain unexplored.

Fetal growth restriction (FGR) affects 5%–8% of human pregnancies (Cotechini et al., 2014; Robb et al., 2017), is associated with a spectrum of perinatal complications (Bezemer et al., 2024), and leads to long-term adverse outcomes, including neurodevelopmental disorders and increased risk of cardiovascular disease in adulthood (Miller et al., 2016). However, in the pig industry, its incidence is even higher, impacting 15%–20% of pregnancies (Li et al., 2018; Van Ginneken et al., 2023). The placenta is a highly specialized organ composed of both maternal (basal plate and decidua) and fetal components (chorioallantoic membrane, amniotic membrane, and villi) in humans (Bezemer et al., 2024). FGR is commonly linked to abnormal placental vascular development and impaired perfusion, which lead to insufficient nutrient and oxygen supply to the fetus (Cotechini et al., 2014; Figueras et al., 2018). Although previous studies have observed an expansion of pro-inflammatory placental macrophages, including maternal decidual macrophages and fetal Hofbauer cells (HBCs), in FGR (Berezhna et al., 2021; Bezemer et al., 2020, 2024; Chu et al., 2019), the specific mechanisms by which placental macrophage dysregulation contributes to FGR pathogenesis remain elusive. The pig serves as a unique and powerful model, as multiple fetuses develop simultaneously within the same uterine environment, with both normally grown and growth-restricted (GR) individuals naturally coexisting in a single litter. This feature minimizes maternal and environmental confounders, thereby providing a rare opportunity to directly investigate the intrinsic cellular and molecular mechanisms underlying FGR.

In this study, we constructed a comprehensive single-cell transcriptomic atlas of fetal pig macrophages across 54 distinct tissues during late gestation. To minimize genetic, age, and environmental variability, all samples were collected from the same litter: 49 tissues from a male fetus and 19 tissues from its female littermate, with 14 overlapping tissues between the two individuals. This design enabled better controlled cross-tissue cell type comparison and provided a clearer view of conserved versus tissue-specific macrophage features. Specifically, we characterized the conservation and heterogeneity of macrophages across distinct tissue contexts, with particular attention to the dichotomous LYVE1^{high}MHCII^{low} and LYVE1^{low}MHCII^{high} subtypes across this broad tissue spectrum. We further explored TFs potentially involved in defining fetal macrophage identity and function within each individual tissue, assessed their conservation from fetal to adult stages, and explored tissue-associated metabolic programs and their links to macrophage function. Additionally, we performed cross-sex and cross-species comparative analyses to evaluate the transcriptomic similarity of fetal macrophages. Finally, we characterized the heterogeneity of HBCs in the context of FGR to gain preliminary insights into their possible roles in this condition. Our study provides a comprehensive foundational framework for understanding fetal macrophage biology and offers a resource that may inform future investigations into their developmental and pathological roles.

MATERIALS AND METHODS

Animals

Pregnant Large White sows and the mated boars were purchased from Taihe Biotechnology Co., Ltd. (China). For the discovery cohort used to construct the cross-tissue fetal pig macrophage atlas, a pregnant sow at gestational day 110 was anesthetized with isoflurane. For the validation cohort, the same anesthetic procedure was performed on another

pregnant sow at gestational day 107. Following anesthesia, fetuses were delivered via midline laparotomy, and fresh tissues were immediately collected for downstream processing. To investigate FGR, chorioallantoic membrane tissues were sampled from five pairs of normal-weight (NW) and GR fetuses derived from three pregnant sows at 107–111 days of gestation. All animal procedures were approved by the Animal Ethics Committee of Jiangxi Agricultural University (Approval No. JXAULL-2021-37 and No. JXAULL-2023-06-07) and conducted in strict accordance with institutional guidelines.

Tissue collection, processing, and single-cell library preparation and sequencing

This study presents a focused analysis of selected tissues from a broader collection of organs/tissues and individuals, with the specific aim of constructing a cross-tissue macrophage atlas in fetal pigs. Specifically, for the discovery cohort used to construct the cross-tissue fetal pig macrophage atlas, we selected 49 tissues from a male fetus (F1S1: $Family_1$ Son_1) and 19 tissues from its full-sibling female fetus (F1D1: $Family_1$ $Daughter_1$). Among these, 14 tissues were shared between the two individuals (F1S1: 49 tissues; F1D1: 19 tissues; overlap: 14 tissues) (Supplementary Figure S1A). For the validation cohort, 13 tissues matching those from F1S1 were collected from a male fetus of a different litter (F2S3: $Family_2$ Son_3) (Supplementary Figure S1A). All fresh tissue samples destined for single-cell suspension preparation were immediately stored on ice in sCelLive™ tissue preservation solution (Singleron Biotechnologies, China) upon collection. For histological and immunofluorescence analyses, tissues were fixed in 10% neutral buffered formalin, and the fixative was replaced after 48 h. Detailed sample information is provided in Supplementary Table S1.

Following tissue collection, enzymatic digestion was performed immediately to prepare single-cell suspensions. Single-cell suspensions were generated using enzyme combinations optimized for each tissue (e.g., collagenase, DNase, dispase) as previously described (Cai et al., 2026; Chen et al., 2025a). Briefly, tissues were minced into small fragments and incubated in tissue-specific enzymatic digestion solutions at 37°C in a shaking water bath (110 r/min) for 25–60 min to promote dissociation. The resulting suspensions were sequentially filtered through 100 μm and 40 μm strainers (Falcon, USA), subjected to red blood cell lysis (BD Biosciences, USA), washed, and counted. Bone marrow tissues (red and yellow) were flushed directly rather than digested enzymatically. PBMCs were isolated using a porcine peripheral blood lymphocyte isolation kit (Solarbio, China). For the brain and pancreas, dissociation was carried out according to the GEXSCOPE tissue dissociation kit protocol (Singleron Biotechnologies, China). Single-cell suspensions derived from each tissue with a cell count exceeding 1×10^5 and a viability rate above 80% were immediately used for single-cell library construction as previously described (Chen et al., 2025a). In brief, single-cell RNA libraries were prepared using the GEXSCOPE® Single Cell RNA Library Kit (Singleron Biotechnologies, China) following the manufacturer's protocol. Specifically, cells were captured and barcoded, and mRNA was reverse-transcribed, followed by cDNA amplification and library construction. Sequencing was performed on an Illumina NovaSeq 6000 system (Illumina, USA).

Single-cell RNA-seq processing, integration and cell type annotation

Raw sequencing reads were processed to generate gene expression profiles using CeleScope v.1.1.8 (Singleron Biotechnologies, China) with default parameters. Briefly, barcodes and unique molecular identifiers (UMIs) were extracted from R1 reads and corrected for errors. Adapter sequences and poly(A) tails were trimmed from R2 reads, and the cleaned R2 reads were aligned to the Sscrofa 11.1 reference genome (Warr et al., 2020) using STARSolo (Kaminow et al., 2021), with gene annotation based on the Sus scrofa GTF file (v.101) from the Ensembl database (Harrison et al., 2024). Reads successfully assigned to the same cell barcode, UMI, and gene were aggregated to construct cell–gene count matrices. Gene symbols for unannotated Ensembl IDs were assigned via BLAST against the UniProt database (The UniProt Consortium, 2015). Quality control was performed independently for each sample in Scanpy v.1.7.1 (Wolf et al., 2018), with cells filtered primarily based on the following criteria: *n*_genes_by_counts<5 000, total_counts<30 000, pct_counts_mt<25, max_genes<5 000, min_genes>300, scrublet_doublet_score<0.25. Additionally, genes detected in fewer than 3 cells were removed. A two-step strategy was adopted for data integration and cell type annotation. First, datasets derived from the same or physiologically similar organs were analyzed independently following a standardized pipeline for normalization, batch correction (implemented via Harmony (Korsunsky et al., 2019), BBKNN (Polański et al., 2020), or FindIntegrationAnchors (Hao et al., 2021)) (Supplementary Table S1), dimensionality reduction, Louvain clustering, and cell type annotation. Cell identities were assigned using CellID (Cortal et al., 2021) with reference markers sourced from PanglaoDB (Franzén et al., 2019), the Human Protein Atlas (https://www.proteinatlas.org/), and relevant literature, followed by manual curation based on cluster-specific differentially expressed genes (DEGs) and canonical cell type markers. Second, organ-level annotated datasets were globally integrated using Scanorama (Hie et al., 2019) (for sample effect correction) and BBKNN (Polański et al., 2020) (for platform correction) in Scanpy v.1.7.1 (Wolf et al., 2018), followed by Louvain clustering (resolution=3). Final annotations were defined using canonical markers, the top 200 DEGs per cluster, and organ-specific references, yielding an integrated single-cell transcriptomic atlas encompassing all cell types across all major organs (Cai et al., 2026).

Extraction of macrophages

From the integrated single-cell transcriptome atlas (as mentioned above) (Cai et al., 2026), macrophages were extracted for focused downstream analysis. Specifically, for the discovery cohort used for cross-tissue fetal pig macrophage atlas construction, we extracted macrophages from one male (F1S1) and one female fetal pig (F1D1) (gestational day 110, same litter) and applied a step-by-step workflow in Scanpy v.1.7.1 (Wolf et al., 2018) to ensure accuracy and robustness, as detailed below. First, we extracted all immune cells (238 039 cells) from the integrated atlas and performed comprehensive annotation using both automated and manual methods. This process identified 13 high-quality immune cell types (Leiden algorithm, resolution=1), which were classified into two major lineages: myeloid and lymphoid (Supplementary Figures S2A–C). Next,

we extracted 134 843 myeloid cells from the re-annotated immune cell atlas and performed further sub-clustering, yielding 27 distinct cell types (Leiden algorithm, resolution=4.5; Supplementary Figure S2D). From this myeloid subset, we extracted 85 473 macrophages derived from 54 tissues for downstream analysis. At each step, tissues with fewer than 50 cells were excluded to ensure robust representation, and potential contaminating cell types were removed based on the expression of the top 200 DEGs and canonical cell type markers. The extracted macrophages were processed for dimension reduction and unsupervised clustering by following the workflow in Scanpy v.1.7.1 (Wolf et al., 2018). In brief, 2 000 highly variable genes (HVGs) were selected using scanpy.pp.highly_variable_genes, followed by regression of total counts per cell and mitochondrial gene percentages via scanpy.pp.regress_out. Genes were scaled to unit variance (scanpy.pp.scale, max_value=10), and a 50-component PCA was computed (scanpy.tl.pca, svd_solver= "arpack"). Batch effects between male and female samples were corrected using Harmony (scanpy.external.pp. harmony_integrate). Neighborhood graphs were constructed (scanpy.pp.neighbors, n_neighbors=15, n_pcs=40, use_rep= "X_pca_harmony"), and UMAP was used for visualization (scanpy.tl.umap). Unsupervised clustering was performed via the Leiden algorithm (resolution=3.5), with DEGs identified using the Wilcoxon rank-sum test (scanpy.tl.rank_genes_ groups). Cell type annotation combined canonical markers from literature, top DEGs, and automated classification via CellTypist v.1.5.1 (Domínguez Conde et al., 2022) (logistic regression models with majority voting). Clusters with significant similarity—sharing >100 of the top 200 DEGs, overlapping tissue origins, or close hierarchical proximity—were merged. Clusters predominantly (>85%) from tissues with established nomenclature (e.g., KCs) retained canonical names; those with mixed origins or undefined classifications were designated by representative DEGs. For the validation cohort, cells annotated as macrophages and derived from a male fetal pig of another litter (F2S3) were extracted from the integrated atlas (as described above) (Cai et al., 2026). We then performed HVG identification (scanpy.pp.highly_variable_genes), PCA (scanpy.pp.scale, max_value=10), and UMAP (scanpy.tl.umap, default parameters) dimensionality reduction, followed by Leiden clustering at a resolution of 0.8. Based on the expression of canonical macrophage markers and DEGs for each cluster, non-macrophage clusters were removed, and tissues containing fewer than 50 cells were excluded. Finally, we obtained a macrophage dataset comprising 7 688 cells across 13 tissues. To verify the reproducibility of the cross-tissue fetal pig macrophage atlas constructed from the discovery cohort, we integrated macrophages from the discovery and validation cohorts using the sc.external.pp.harmony_integrate function to correct for batch effects.

Diversity analysis of macrophage subtype composition

To quantify the diversity of macrophage subtype composition among tissues, the normalized Shannon equitability index (E_H; Zheng et al., 2021) E_H was calculated as:

$$E_H = \frac{-\sum_{i=1}^{N} p_i log_2 p_i}{log_2 N} \quad (1)$$

where p_i is the frequency of subtype i, and N is the total number of subtypes. The Shannon equitability index ranges from 0 to 1, with higher values indicating greater diversity.

Functional enrichment analysis

Functional enrichment analysis was performed using the clusterProfiler v.4.10.0 package (Yu et al., 2012). Multiple testing correction was applied via the Benjamini-Hochberg method, with pathways considered significantly enriched at a P<0.05.

Principal component analysis of cross-tissue LYVE1^{high}MHCI^{low} and LYVE1^{low}MHCII^{high} subtypes

To investigate the cross-tissue transcriptional conservation of the dichotomous macrophage subtypes (LYVE1^{high}MHCII^{low} and LYVE1^{low}MHCII^{high}), we performed principal component analysis (PCA) using the following analytical strategy. First, within each of the 27 target tissues, the two subtypes were independently annotated based on the expression patterns of *LYVE1*, MHC class II genes (e.g., *SLA-DRA*, *SLA-DQB1*, *SLA-DRB1*), and cluster-specific DEGs. For each tissue with both subtypes, the corresponding cells were extracted and merged into a combined dataset. To mitigate the impact of data sparsity inherent in single-cell transcriptomics, the top 2 000 HVGs were identified from this merged dataset. Subsequently, the mean expression profiles of these 2 000 HVGs across all tissue-subtype groups were subjected to PCA using the prcomp function in R software v.4.3.2 with default parameters. The first two principal components (PC1 and PC2) were extracted to evaluate the clustering patterns of the subtypes across different tissues.

Evaluation of the conservation of LYVE1^{high}MHCII^{low} and LYVE1^{low}MHCII^{high} subtypes in humans

To assess the conservation of dichotomous macrophage characteristics between pigs and humans, we downloaded three publicly available human single-cell transcriptomic datasets (Eraslan et al., 2022; Han et al., 2020; Suo et al., 2022) and performed subcluster annotation on macrophages isolated from each tissue.

Subsequently, tissues (lung, muscle, kidney, and heart) shared by pigs and humans were selected, and MetaNeighbor (Crow et al., 2018) was used to evaluate the similarity between the dichotomous subtypes of macrophages in the two species. Pig MHC class II genes (e.g., *SLA-DRA*, *SLA-DQB1*) were manually converted to their human orthologs (e.g., *HLA-DRA*, *HLA-DQB1*).

For gene list enrichment scoring, a pig dichotomous macrophage signature gene list was generated based on DEGs shared across 14 of the 27 tissues (Supplementary Table S2). Pig genes were mapped to their human orthologs using the UniProt database, and then this gene list was applied to each human tissue dataset using the scanpy.tl.score_genes function in Scanpy v.1.7.1 (Wolf et al., 2018) with default parameters (ctrl_size=50, n_bins=25).

Cross-species analysis of fetal macrophages

To assess the conservation of fetal macrophage characteristics across pigs, humans, and mice, we downloaded single-cell transcriptomic datasets for human (Han et al., 2020) and mouse (Fei et al., 2022). Fetal macrophages were isolated from these public datasets and integrated with fetal pig macrophages from matching tissues in the present study using the FindIntegrationAnchors function in Seurat v.4.1.1 (Hao et al., 2021). Following HVG selection and dimensionality reduction, cells were clustered using the Louvain algorithm with a resolution of 0.5.

Gene regulatory network analysis

Gene regulatory networks were inferred using pySCENIC v.0.12.1 (Domínguez Conde et al., 2022), which reconstructs TF-target interactions through a three-step analytical pipeline. First, co-expression modules between TFs and their potential target genes were identified using the GRNBoost2 algorithm, with input gene expression matrices and a curated list of human TFs obtained from https://github.com/aertslab/pySCENIC/blob/master/resources/hs_hgnc_tfs.txt. The resulting modules were subjected to motif enrichment analysis against two cisTarget databases (https://resources.aertslab.org/cistarget/databases/homo_sapiens/hg38/refseq_r80/mc_v10_clust/gene_based/) to identify direct TF-target interactions, retaining only regulons containing at least 10 genes. Finally, regulon activity was quantified across individual cells using AUCell scoring, and regulon cell-type specificity was evaluated by calculating regulon specificity scores (RSS), enabling the identification of cell-type-specific regulatory programs.

Identification of tissue-specific and tissue-shared transcription factors

A total of 1 232 pig TFs were obtained from the JASPAR database (https://jaspar.elixir.no/) and used for downstream analysis. To identify TFs shared across tissues, a TF was classified as tissue-shared if it was detected in over 80% of tissues and expressed in more than 5% of cells within a tissue. Tissue-shared TFs in the fetal and adult stages were then identified separately.

To identify tissue-specific TFs, the gene specificity index (Tau, τ) for each TF was computed as described by Yanai et al. (2005). The index was calculated as follows:

$$\tau = \frac{\sum_{i=1}^{N}(1-\hat{x}_i)}{N-1}$$

$$\hat{x}_i = \frac{x_i}{max(x_i)} \quad (2)$$

where N is the number of tissues (N=54 in this study) and x_i represents the average normalized gene expression of a given tissue i, τ represents the gene specificity score for the tissue, with values ranging from 0 to 1; higher values indicate stronger tissue specificity. A TF was classified as tissue-specific if it met the following criteria: (1) τ>0.85, (2) average expression≥0.05, and (3) expression in≥5% of cells within the dominant tissue. Consistent with the analysis of shared TFs, tissue-specific TFs were identified separately for fetal and adult stages.

Gene set scoring analysis

Gene set scoring was performed for 42 metabolic pathways (Kyoto Encyclopedia of Genes and Genomes (KEGG) database; Supplementary Table S3), 43 macrophage-related functional pathways (KEGG/Gene Ontology (GO)/Reactome databases; Supplementary Table S3), and 32 immune activity pathways (KEGG/GO/Reactome databases; Supplementary Table S4). Enrichment scores for each gene set in individual cells were computed using the scanpy.tl.score_genes function in Scanpy v.1.7.1 (Wolf et al., 2018) with default parameters (ctrl_size=50, n_bins=25). For the metabolic and functional pathway scoring analyses, specific Ensembl IDs were manually curated and updated for the following reasons: initial gene symbols assigned via BLAST alignment against the UniProt database were incomplete or ambiguous, often resulting in truncated or outdated nomenclature; and certain Ensembl IDs, whose gene symbols were absent from the initial annotation file, could be retrieved from the UniProt database. A comprehensive list of these corrected genes is provided in Supplementary Table S3.

Integration of macrophage datasets from fetal and adult pigs

The fetal pig macrophage atlas (present study) and adult pig macrophage atlas (our previously published dataset) (Chen et al., 2025a) were integrated using the FindIntegrationAnchors function in Seurat v.4.1.1 (Hao et al., 2021).

Definition of fetal growth restriction

Fetuses were classified as GR when their body weights were below one standard deviation of the population mean both within the litter and across the population. This empirical cutoff was determined from 860 sixth-generation (F6) mosaic pigs (Yang et al., 2022), among which individuals were grouped into NW and GR groups according to different cutoff values below the population mean of birth weight (ranging from 1.0 to 2.0 standard deviations). The criterion of one standard deviation below the mean resulted in the greatest difference in body weight between the two groups at 240 days of age and was therefore used to define intrauterine growth restriction in this study.

Macrophages from normal-weight and growth-restricted fetal pigs

Macrophages were extracted from our previously generated chorioallantoic membrane single-cell transcriptomic dataset (Cai et al., 2026), which included samples from five NW and five GR fetuses. The macrophage subtypes were subjected to downstream analyses, including normalization, dimensionality reduction, and identification of DEGs. In brief, 2 000 HVGs were selected using scanpy.pp.highly_variable_genes, followed by regression of total counts per cell and mitochondrial gene percentages via scanpy.pp.regress_out. Genes were scaled to unit variance (scanpy.pp.scale, max_value=10), and a 50-component PCA was computed (scanpy.tl.pca, svd_solver="arpack"). Experimental batch effects, litter variations, and individual differences were corrected using Harmony (scanpy.external.pp.harmony_integrate). Neighborhood graphs were constructed (scanpy.pp.neighbors, n_neighbors=15, n_pcs=40, use_rep="X_pca_harmony"), and UMAP was used for visualization (scanpy.tl.umap). DEGs between NW and GR conditions were computed using the Wilcoxon rank-sum test (scanpy.tl.rank_genes_groups).

Integration of the cross-tissue fetal pig macrophage atlas and the FGR macrophage dataset

To clarify the correspondence between macrophage subtypes in the cross-tissue fetal pig macrophage atlas and those in the FGR dataset, we integrated the FGR dataset with the cross-tissue fetal pig macrophage atlas using the FindIntegrationAnchors function in Seurat v.4.1.1 (Hao et al., 2021). We then assessed the similarity by calculating Pearson correlations between the average gene expression profiles of NW and GR macrophages and those of each subtype in the cross-tissue fetal pig macrophage atlas.

Cell-cell communication analysis

Intercellular communication analysis was performed using the

CellChat R package (v.1.1.3) (Jin et al., 2021) with default parameters, retaining only significant ligand-receptor interactions (P<0.05) between cell populations containing ≥10 communicating cells for downstream analyses.

Immunofluorescence staining and imaging

Paraffin-embedded tissues were cut into sections with a thickness of 3–5 μm using a microtome (Leica, Germany) and mounted on glass slides. Sections were deparaffinized in xylene and rehydrated through a graded ethanol series, followed by antigen retrieval and serum blocking. For double immunofluorescence staining, tissue sections were incubated overnight at 4°C with mouse anti-CD163 (ab156769, Abcam, UK). This antibody was combined with rabbit anti-C1orf85 (ab231317, Abcam, UK) for amniotic membrane sections and with rabbit anti-NR4A3 (55405-1-AP, Proteintech, USA) for tonsil sections. After three washes with PBS (pH 7.4), sections were incubated with Cy3-conjugated goat anti-mouse IgG (GB21301, Servicebio, China) and Alexa Fluor 488-conjugated goat anti-rabbit IgG (GB25303, Servicebio, China) for 50 min. Following three additional PBS (pH 7.4) washes, nuclei were stained with DAPI, and sections were mounted. Multispectral images were acquired using a Pannoramic MIDI scanner and analyzed with CaseViewer software (v.2.4).

RESULTS

A fetal pig macrophage cross-tissue single-cell transcriptome atlas

To comprehensively characterize the cross-tissue heterogeneity of macrophages in fetal pigs, we extracted macrophages from our previously established multi-tissue integrated single-cell atlas (Cai et al., 2026) by sequentially isolating and annotating immune cells, re-clustering myeloid cells, and finally extracting macrophages (Supplementary Figures S2A–D). After stringent quality control, 85 473 macrophages from 54 distinct tissues were obtained for downstream analysis, including 49 tissues from a male fetal pig and 19 tissues from its female littermate, with an overlap of 14 tissues between the two individuals (Figure 1A; Supplementary Figure S1A and Table S1). These cells were unequivocally identified as macrophages based on their robust expression of canonical markers, including *CD68*, *CD163*, *MRC1*, *C1QB*, *CSF1R* and *CX3CR1* (Chen et al., 2011; Rakina et al., 2024), as well as the minimal to absent expression of markers for other myeloid cell types (Figure 1B; Supplementary Figure S2E).

Unsupervised clustering following dimensionality reduction identified 15 macrophage subtypes with distinct transcriptional signatures and tissue distributions (Figures 1C–E; Supplementary Table S1). Several subtypes corresponded to known tissue-specific macrophage subtypes, such as MG and border-associated macrophages (BAMs) in the central nervous system expressing *CALCR* and *CD163*, respectively; KCs in the liver expressing *ID3*; and RPMs in the spleen expressing *SPIC* (Blériot et al., 2020; Gordon & Plüddemann, 2017; Li & Barres, 2018). Within placental-associated tissues, we identified two HBC subtypes, both expressing canonical markers *SPP1*, *CD14*, *CD68*, *CD163* and *FOLR2* (Supplementary Figure S3A) (Thomas et al., 2021; Yang et al., 2023), yet distinguished by their tissue distribution and functional programs. HBC GPNMB+ cells were restricted exclusively to the amniotic membrane and highly expressed glycolytic enzymes (*LDHA*, *ENO1*) and extracellular matrix (ECM) regulators (*GPNMB*, *ANXA2*, *COL1A1*) (Supplementary Figure S3A and Table S1). In contrast, HBC PEG10+ cells resided solely in the chorioallantoic membrane and highly expressed immunomodulators (*A2M*, *CCL24*), along with *MEF2C* (a key transcriptional regulator of myeloid differentiation) and *PEG10* (an imprinted gene controlling placental development) (Supplementary Figure S3A and Table S1). Notably, this tissue-specific organization was consistently reproduced across two individuals (Supplementary Figure S3B). GO enrichment analysis of DEGs revealed that HBC GPNMB+ cells were enriched for terms related to ECM organization, wound healing, and pyruvate metabolic processes, whereas HBC PEG10+ cells were associated with interleukin-2 production, immune response-activating signaling pathway, and cell cycle G1/S phase transition, suggesting functional adaptation to their respective placental niches (Supplementary Figures S3C, D and Table S1).

In contrast to these tissue-specific subtypes, two macrophage subtypes with broad tissue distribution were further delineated. Mφ CXCL2+ cells exhibited high expression of *SLA-DQB1*, *SLA-DRA*, *CCL4* and *CXCL2*, while Mφ CCL14+ cells were characterized by elevated expression of *CCL14*, *LYVE1* and *DAB2*. Both subtypes were widely populated across multiple systems, including cardiovascular, reproductive, respiratory, urinary, and digestive systems (Figure 1E). Additionally, we identified two proliferative macrophage subtypes, both exhibiting high expression of cell cycle regulators such as *CENPE*, *CENPF*, and *TOP2A*. Proliferating microglia (Prolif MG) were almost restricted to the brain, while proliferating macrophages (Prolif Mφ) were predominantly distributed across peripheral tissues, particularly the chorioallantoic membrane, epididymis, salivary gland, and large intestine, indicating their active expansion during fetal development (Figure 1E; Supplementary Table S1). Quantitative assessment of cell composition diversity using the Shannon equitability index (Zheng et al., 2021) demonstrated significantly greater macrophage diversity in digestive and immune systems compared to other systems (Figure 1E), reflecting the heightened microenvironmental complexity of these tissues during fetal development.

To further clarify the relationships among macrophage subtypes, we performed hierarchical clustering of these subtypes based on their transcriptomic expression profiles, followed by GO functional enrichment analysis to characterize functional programs. This analysis grouped the subtypes into four major clusters with distinct biological specializations (Figure 1F; Supplementary Table S1): Cluster I (Mφ CXCL2+, Mφ MYL1+, and Mφ MYL2+) was associated with inflammatory response and antigen presentation; Cluster II (HBC GPNMB+, BAMs, HBC PEG10+, and Mφ CCL14+) exhibited signatures of extracellular structure organization and tissue remodeling processes; Cluster III (KCs, Mφ CD209+, RPMs, Mφ MARCO+, and Mφ DNASE1L3+) was enriched for purine nucleoside triphosphate biosynthetic process and response to lipopolysaccharide; and Cluster IV (MG, prolif Mφ, and prolif MG) showed enrichment in neuronal development and cell cycle processes.

To verify the reliability of our fetal pig cross-tissue macrophage atlas, we incorporated macrophage single-cell transcriptomic data from 13 replicate tissues of an independent male fetus from a different litter (Supplementary Figure S1A), and subsequent integration with the discovery

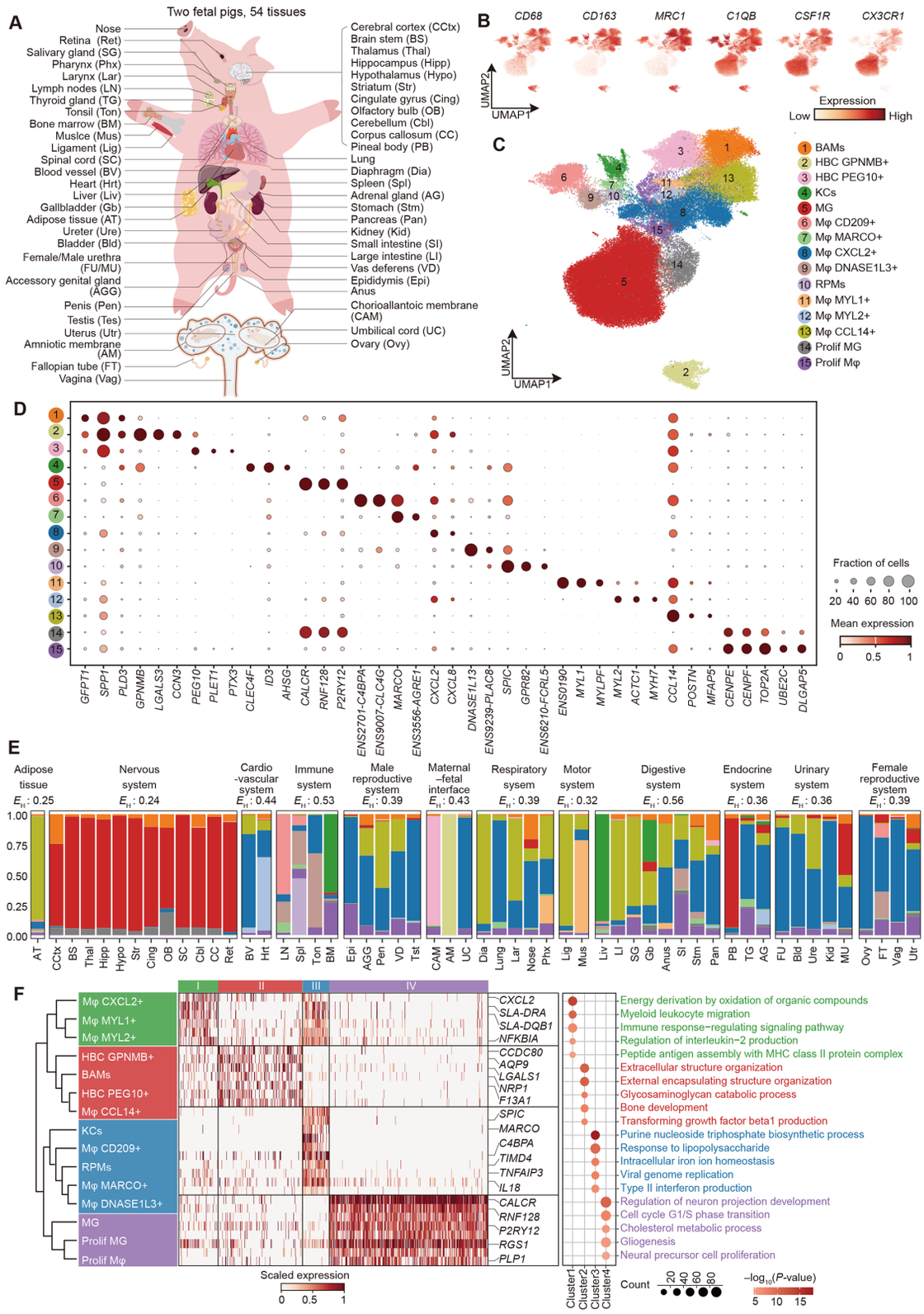


Figure 1 Characteristics of cross-tissue fetal pig macrophages

A: A schematic diagram of 54 sampled tissues from two fetal pigs. B: UMAP showing the expression levels of 6 selected macrophage marker genes. C: UMAP visualization of macrophages colored by 15 macrophage subtypes. D: Dot plot showing signature gene expression profiles across 15 macrophage subtypes. Color intensity represents scaled mean normalized expression levels, while dot size corresponds to the percentage of cells expressing each gene within a subtype. E: Bar plots showing the macrophage subtype proportions across tissues in different systems. Subtype diversity measured with the Shannon equitability index for each system is shown. F: Molecular and functional characterization of macrophage subclusters. Left: Unsupervised hierarchical clustering of macrophage subtypes based on gene expression patterns, revealing four distinct clusters. Middle: Heatmap of cluster-defining signature genes. Representative genes are labeled on the right. Right: Bubble plot of significantly enriched GO pathways (*P*-adjust<0.05) specific to each cluster.

cohort demonstrated favorable clustering of macrophages across both datasets (Supplementary Figures S4A–C). Furthermore, the macrophage subtypes identified across the 13 tissues in the validation cohort, together with their relative proportions and gene expression profiles, were highly concordant with those in the discovery cohort (Supplementary Figures S4D, E). Together, the concordant cell identity features observed across individuals further validate the reproducibility and robustness of our cross-tissue macrophage atlas.

Conserved cross-tissue dichotomy of LYVE1^{high} and MHCII^{high} macrophages

Previous studies have identified two transcriptionally distinct macrophage subtypes, LYVE1^{high}MHCII^{low} and LYVE1^{low}MHCII^{high}, with dichotomous expression patterns across tissues of humans, mice, and zebrafish (Chakarov et al., 2019; Eraslan et al., 2022; Lund et al., 2024; Zhou et al., 2023a). Here, leveraging the comprehensive cross-tissue single-cell atlas in pigs, we systematically explored these two subtypes in each individual tissue to comprehensively characterize their transcriptional programs and assess their similarity to their human counterparts. Our analysis revealed that these transcriptionally mutually exclusive subtypes were widely conserved across fetal pig tissues, being consistently observed in 27 of the 54 examined tissues (Supplementary Figure S5A).

Through cross-tissue analysis of conserved transcriptomic features, we identified the core signatures for each subtype. Specifically, LYVE1^{high} macrophages preferentially expressed genes involved in tissue remodeling and homeostasis (*LYVE1*, *DAB2*, *MRC1*), whereas MHCII^{high} macrophages were characterized by elevated expression of antigen presentation components (*SLA-DQB1*, *SLA-DRA*, *SLA-DRB1*) (Figure 2A; Supplementary Table S2). Notably, within each tissue, the expression levels of *LYVE1* and MHC class II genes (*SLA-DRA*, *SLA-DRB1* and *SLA-DQB1*) showed a significant negative correlation (Spearman's $r \leq -0.18$, $P<0.001$) (Supplementary Figures S5A, S6A–D), and this inverse relationship was further validated in our independent validation cohort (Supplementary Figure S7A). Despite maintaining their core molecular signatures, both macrophage subtypes displayed tissue-specific expression profiles and varying abundance proportions (Supplementary Figures S8A, B), reflecting adaptation to distinct tissue microenvironments. PCA further revealed that PC1 and PC2 clearly segregated the two subtypes across diverse tissues (Figure 2B). In addition, GO functional analysis highlighted the functional divergence between the two macrophage subtypes. LYVE1^{high} macrophages were enriched for pathways including receptor-mediated endocytosis, TGFβ response, cell-matrix adhesion, and epithelial cell migration, consistent with their proposed functions in tissue maintenance and repair (Chakarov et al., 2019). In contrast, MHCII^{high} macrophages showed strong enrichment for immune activation pathways, particularly antigen processing and presentation (Figure 2C; Supplementary Table S2).

Given the widespread conservation of the dichotomous macrophage subtypes across tissues, we next sought to identify the transcriptional regulators underlying their functional and identity specialization via pySCENIC analysis (Van De Sande et al., 2020). We identified MAF(+) and RBPJ(+) as key regulons specifically associated with the LYVE1^{high} subtype, both of which exhibited high regulon specificity scores (RSS>0.5) and consistently showed higher AUCell scores in LYVE1^{high} than in MHCII^{high} macrophages across nearly all examined paired tissues (Figure 2D; Supplementary Table S2). Notably, both of these TFs and their predicted target genes (*CLTC* for *MAF*; *ITSN1* and *COLEC12* for *RBPJ*) showed coordinated and specific high expression in LYVE1^{high} macrophages (Figure 2E), indicating functionally relevant regulatory relationships. Consistent with our findings, Moura Silva et al. demonstrated that *Maf* acts as a pivotal regulator in establishing the identity and function of LYVE1+ perivascular macrophages (2021), further supporting its conserved role in sustaining LYVE1^{high} macrophage programs.

To assess the evolutionary conservation of these macrophage specializations, we performed cross-species comparisons between pigs and humans using MetaNeighbor (Crow et al., 2018). Remarkably, pig LYVE1^{high} and MHCII^{high} macrophages (P_LYVE1^{high} and P_MHCII^{high}) showed strong transcriptional similarity to their human counterparts (H_LYVE1^{high} and H_MHCII^{high}) across all examined tissues, respectively (Figure 2F). Furthermore, specific regulons identified in pigs were also conserved in some human tissues, such as the chorionic villus and placenta (Figure 2G). To further validate this conservation, we generated a list of pig dichotomous macrophage signature genes based on DEGs shared across 14 out of 27 tissues (Supplementary Table S2), and applied it to human datasets. The results revealed significant enrichment of the pig LYVE1^{high} signature in human LYVE1^{high} macrophages ($P<0.001$, Wilcoxon test), with similar findings for the MHCII^{high} macrophages (Supplementary Figure S9A), providing compelling evidence for the fundamental nature of this macrophage specialization across species. Collectively, these results establish the LYVE1^{high} and MHCII^{high} dichotomy as a widely tissue-distributed and conserved macrophage state during late gestation, characterized by distinct transcriptional programs, regulatory mechanisms, and functional roles that are highly analogous to those observed in human tissue macrophages.

Metabolic heterogeneity of macrophages across tissues

Cellular metabolism dynamically reprograms the phenotypes and functions of immune cells, exemplified by its central roles in T cell differentiation (Buck et al., 2015) and macrophage polarization (Wculek et al., 2022). To explore the metabolic programs underlying macrophage maintenance and tissue adaptation, we analyzed the expression of 1 346 metabolism-related genes encompassing 42 KEGG metabolic pathways in macrophages across 54 tissues (Supplementary Table S3). Among these, 247 genes were ubiquitously expressed in over 80% of tissues (detected in >5% of cells per tissue), with notable enrichment in OXPHOS, reactive oxygen species (ROS) metabolism, and the tricarboxylic acid (TCA) cycle (Figure 3A). This enrichment pattern was recapitulated in the validation cohort (Supplementary Figure S10A). Together, these findings suggest that fetal macrophages share a conserved metabolic program centered on mitochondrial respiration and redox homeostasis, which may provide the energetic and biosynthetic support required for their survival and function.

Beyond this conserved metabolic foundation, macrophages exhibited striking tissue-specific specialization. Among all tissues, macrophages from the amniotic membrane exhibited

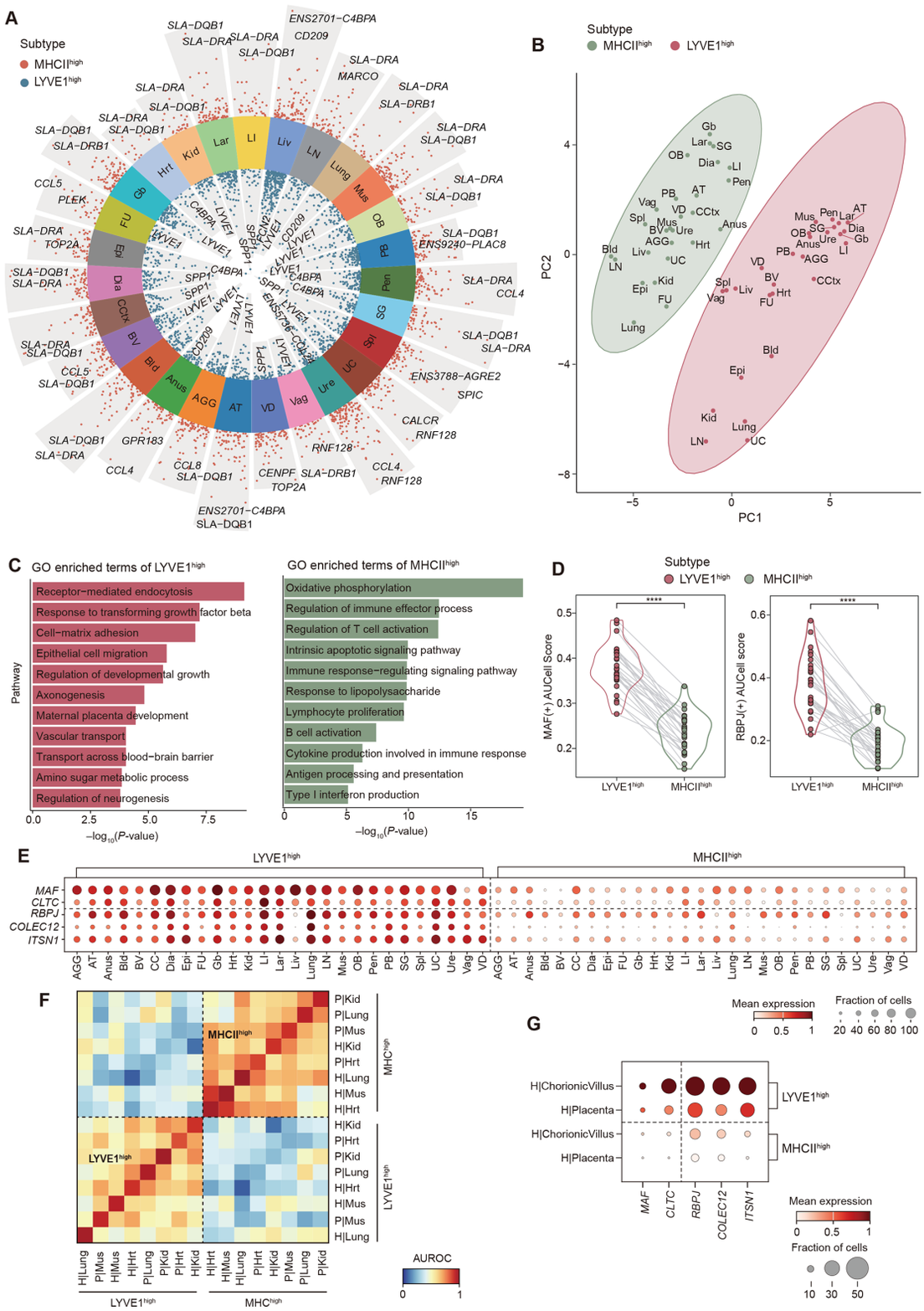


Figure 2 A macrophage dichotomy across tissues and its conservation in human tissues

A: Volcano plot displaying DEGs between LYVE1^{high}MHCII^{low} and LYVE1^{low}MHCII^{high} macrophage subtypes across 27 tissues. Genes meeting the thresholds (|$\log_2$(fold change)|>1 and *P*-adjust≤0.05) are colored, with top genes labeled in the plot. B: PCA analysis of gene expression patterns in LYVE1^{high}MHCII^{low} and LYVE1^{low}MHCII^{high} macrophage subtypes from 27 tissues. C: GO terms of the DEGs in LYVE1^{high}MHCII^{low} and LYVE1^{low}MHCII^{high} macrophage subtypes. D: Violin plots comparing the average AUCell scores of MAF(+) (left) and RBPJ(+) (right) regulons between LYVE1^{high}MHCII^{low} and LYVE1^{low}MHCII^{high} subtypes in each paired tissue. Symbols correspond to significance: ****: *P*<0.0001. E: Dot plot showing expression of two regulons (TF and its target genes) in LYVE1^{high}MHCII^{low} and LYVE1^{low}MHCII^{high} macrophage subtypes across 27 tissues. Top: MAF(+) regulon (TF: *MAF*; target: *CLTC*). Bottom: RBPJ(+) (TF: *RBPJ*; targets: *COLEC12*, *ITSN1*). F: Heatmap showing the correspondence of LYVE1^{high}MHCII^{low} and LYVE1^{low}MHCII^{high} macrophage subtypes between pigs and humans, quantified by MetaNeighbor (mean AUROC scores). G: Dot plot showing expression patterns of the two regulons (identified in Figure 2E) in human tissues.

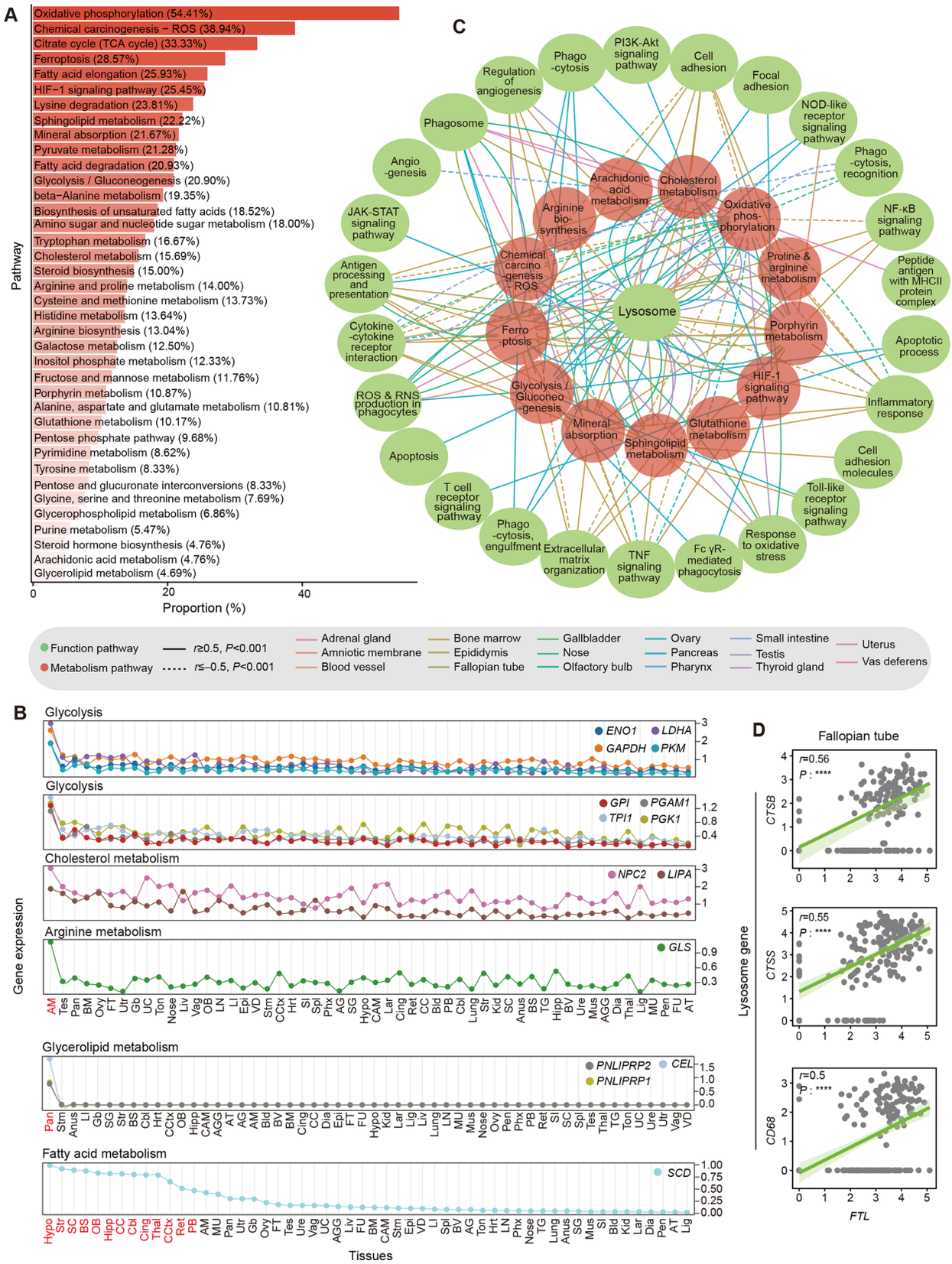


Figure 3 Cross-tissue metabolic transcriptional characteristics

A: Bar plot showing the percentage of ubiquitously expressed genes belonging to 42 KEGG metabolic pathways across 54 tissues. B: Line plot showing expression profiles of 15 selected metabolic genes across 54 tissues. C: Network visualization of significant Spearman correlations (|*r*|≥0.5, *P*<0.05) between macrophage metabolic (red nodes) and functional (green nodes) pathway activities. Solid edges: positive correlations (*r*≥0.5); dashed edges: negative correlations (*r*≤–0.5). Edge colors denote tissue origins. Symbols correspond to significance: ****: *P*<0.0001. D: Scatter plot showing positive correlation in co-expression patterns between the iron metabolic gene and lysosomal function-related genes in fallopian tube macrophages.

the most active metabolic profile, characterized by prominent engagement in glycolysis, cholesterol metabolism, and arginine metabolism (Supplementary Figure S11A). Consistently, they showed high expression of multiple metabolic genes, such as glycolytic regulators (*GAPDH*, *LDHA*, *TPI1*, and *PGAM1*), lipid metabolism-related genes (*LIPA* and *NPC2*), and *GLS*, a key gene for arginine precursor supply (Figure 3B). Pancreatic macrophages showed higher expression of genes involved in glycerolipid metabolism, including *CEL*, *PNLIPRP1*, and *PNLIPRP2* (Figure 3B). Liver and lymph node macrophages exhibited prominent arachidonic acid and iron metabolism (Supplementary Figure S11A), accompanied by high expression of the arachidonic acid enzyme *HPGD* and the iron regulators *HMOX1* and *SLC40A1* (Supplementary Figure S12A), a pattern consistently observed in the validation cohort (Supplementary Figure S10B). Bone marrow macrophages were enriched in nucleotide metabolism and displayed elevated expression of genes involved in this pathway, such as *HPRT1* and *DUT* (Supplementary Figures S11A, S12A). Specifically, macrophages from various brain regions displayed relatively homogeneous metabolic profiles, which aligns with a previous study indicating that, with the exception of the intestines, macrophages within the same tissue or location are largely homogenous regarding their metabolism (Supplementary Figure S11A) (Heieis et al., 2023). These brain macrophages exhibited high lipid metabolic activity and elevated expression of *SCD* (Figure 3B), a fatty acid desaturase that is crucial for driving microglial phenotypic switching by regulating membrane fluidity (Bogie et al., 2020; Hamilton et al., 2022; Sun et al., 2025).

To further explore the relationship between metabolic profiles and macrophage functional characteristics, we scored individual macrophages against gene sets corresponding to 42 metabolic pathways and 43 functional pathways (Supplementary Figures S11A, B), followed by quantification of the pairwise correlations between these metabolic and functional pathway scores in each tissue (Figure 3C; Supplementary Table S3). We identified a negative correlation between OXPHOS and inflammatory pathways in several tissues, including the small intestine, nose, and bone marrow (Supplementary Figure S13A). This finding supports previous in vitro studies showing that OXPHOS is associated with anti-inflammatory macrophages, whereas pro-inflammatory subsets rely on glycolysis (Saha et al., 2017; Wculek et al., 2023). A prominent finding was that lysosomal activity appeared to be a central functional feature of macrophages, as robust associations were observed between lysosomal activity and multiple metabolic pathways across tissues (Figure 3C). For example, pathways involved in iron metabolism, including ferroptosis, mineral absorption, and porphyrin metabolism, showed significant positive correlations (Spearman's $r \geq 0.5$, $P < 0.001$) with lysosomal activity across tissues, such as the nose, fallopian tube, and bone marrow (Supplementary Figure S14A). This correlation was also evident at the gene expression level. Specifically, in fallopian tube macrophages, the iron metabolism gene *FTL* exhibited a strong positive correlation (Spearman's $r \geq 0.5$, $P < 0.001$) with lysosome-related genes (*CTSB*, *CTSS* and *CD68*) (Figure 3D), a pattern consistently observed across other tissues (Supplementary Figure S14A). These findings highlight the critical role of lysosomes as key hubs for iron processing in macrophage-mediated systemic iron homeostasis (Rizzollo et al., 2021). Similarly, lipid metabolism pathways, such as cholesterol and sphingolipid metabolism, were positively correlated with lysosomal function (Supplementary Figure S14A), as evidenced by the co-variation of lipid metabolism genes (*ASAH1*, *LIPA*, and *APOE*) with lysosomal hydrolase genes (Spearman's $r \geq 0.5$, $P < 0.001$), particularly in pancreatic and bone marrow macrophages (Supplementary Figure S14A), aligning with the central role of lysosomes in lipid degradation (Melo & Dvorak, 2012). Notably, the centrality of lysosomal function in macrophages was further corroborated in the validation cohort (Supplementary Figure S10C), where significant correlations (Spearman's $r \geq 0.5$, $P < 0.001$) were observed in both pathway scores and gene expression levels (Supplementary Figure S14B).

Taken together, fetal macrophages showed tissue-specific metabolic adaptations, and different metabolic pathways exhibited distinct correlations with cellular functions, reflecting coordinated metabolic–functional coupling across tissues.

Sex comparison in fetal pig macrophages across tissues

Our within-litter experimental design, in which all samples were collected from a male and a female fetus within the same uterus, minimizes confounding variables such as environment, gestational age, and genetic background, thereby facilitating comparisons of macrophages between sexes across tissues. We systematically compared 14 shared tissues (11 nervous system tissues and 3 other tissues) between male and female fetal pigs. Both the major macrophage subtypes and their relative abundances were largely consistent between sexes within each tissue (Figure 4A). Pearson correlation analysis of the gene expression profiles of all major subtypes across the overlapping tissues further revealed a high degree of transcriptional similarity between male and female macrophages (Figure 4B). GO enrichment analysis of sex DEGs across all tissues revealed that functional differences between sexes were primarily reflected in fundamental metabolic pathways and basic immune functions (Figure 4C). For example, in the amniotic membrane, male macrophages predominantly upregulated processes such as oxidative phosphorylation and other aerobic respiratory processes, represented by genes such as *ATP5ME*, *NDUFA4*, and *COX6A1*, whereas female macrophages showed increased expression of genes involved in wound healing and myeloid cell differentiation, including *ANXA2*, *CD44*, and *HIF1A*. In contrast, in the umbilical cord, male macrophages showed enrichment for immune-related pathways such as myeloid leukocyte migration and monocyte chemotaxis, while female macrophages exhibited enrichment for aerobic respiration and ATP metabolic processes. These results indicate that sex differences among fetal pig macrophages from the same litter during late pregnancy are subtle at the global transcriptomic level, with specific functional divergences primarily confined to fundamental metabolic and immune processes.

Dynamics of macrophage transcriptional programs across fetal and adult tissues

To characterize the spatiotemporal heterogeneity of macrophage transcriptional and functional programs across fetal and adult stages, we integrated the single-cell transcriptomic atlas of fetal pig macrophages generated in this study with our previously published multi-tissue macrophage atlas from adult pigs (Chen et al., 2025a). The integrated UMAP visualization revealed a well-mixed distribution of fetal and adult macrophages, and hierarchical clustering showed

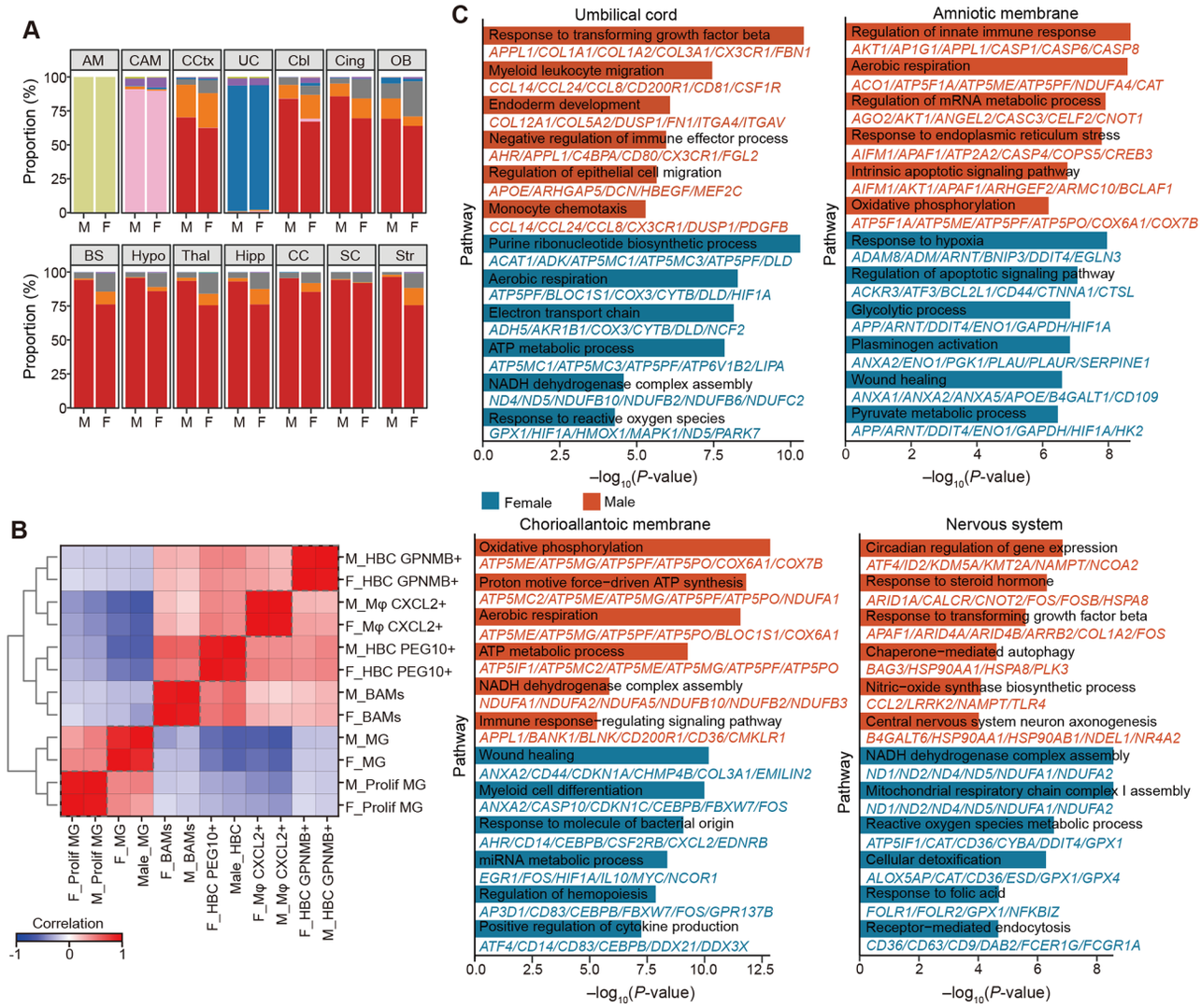


Figure 4 Cross-sex transcriptional characteristics

A: Bar plots showing the proportions of macrophage subtypes across 14 overlapping tissues between male and female pigs. Colors correspond to the macrophage subtypes referenced in Figure 1C. B: Heatmaps showing the Pearson correlation of major subtypes from overlapping tissues between male and female pigs. C: Bar plots showing the GO terms enriched in genes upregulated in males and females across 4 tissues.

that most macrophage subtypes from both stages clustered together (Figure 5A; Supplementary Figures S15A–C). This observation indicated robust dataset integration, thereby enabling accurate cross-stage comparative analyses.

To elucidate the global transcriptional and functional heterogeneity between fetal and adult macrophages, we first aggregated macrophages across all fetal tissues and compared them with those from all adult tissues (Figure 5B; Supplementary Table S4). Adult macrophages showed prominent enrichment in immune-related pathways, including the regulation of immune effector processes and leukocyte cell–cell adhesion, together with fatty acid metabolic processes, reflecting enhanced immune surveillance and regulatory activities within mature tissue environments. In contrast, fetal macrophages primarily exhibited strong enrichment in development-associated pathways, such as the regulation of leukocyte proliferation, myeloid cell differentiation, in utero embryonic development, and cell–substrate junction organization, reflecting their active involvement in immune cell development and tissue morphogenesis during ontogeny. Considering that TRMs originate from the embryonic yolk sac or fetal liver, colonize their respective tissues before birth, and persist postnatally through self-renewal under steady-state conditions (Figure 5C), we next examined whether this developmental divergence persists within representative TRM subtypes (KCs, BAMs, RPMs, and MG) (Schulz et al., 2012; Yona et al., 2013). Consistent with the results observed at the whole-tissue level, these subtype-specific analyses further revealed a conserved shift of TRMs from developmental programs in the fetal period to immune-competent phenotypes in adulthood. Specifically, adult KCs, BAMs, and MG were enriched for antigen processing and presentation, leukocyte activation, cytokine production, and other immune effector pathways, indicative of their acquisition of mature host defense capacities upon environmental exposure after birth (Figure 5D; Supplementary Figure S15D). In contrast, fetal TRMs across tissues preferentially upregulated programs related to cellular proliferation/differentiation and tissue morphogenesis, such as mononuclear cell proliferation in RPMs, myeloid cell homeostasis in KCs, cell migration/adhesion in BAMs, and regulation of neurogenesis in MG, reflecting their roles in organogenesis and niche establishment during development (Figure 5D; Supplementary

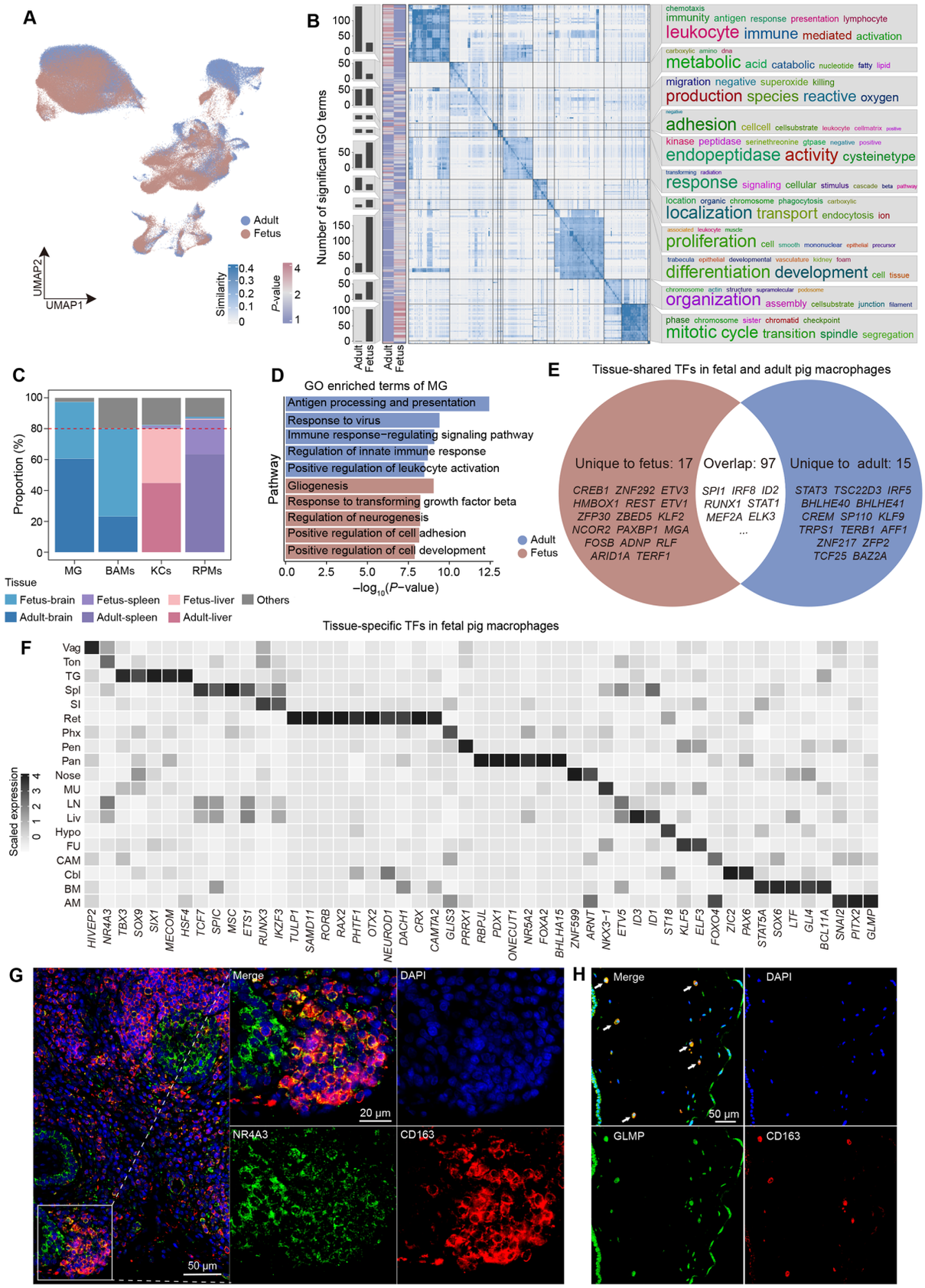


Figure 5 Transcriptional programs in fetal versus adult macrophages

A: UMAP visualization of integrated fetal and adult pig macrophages. B: Clustering and word cloud analysis of GO enrichment results for DEGs between fetal and adult macrophages. C: Bar plot illustrating the tissue distribution of the four TRM subtypes. D: GO terms of DEGs in fetal versus adult MG. E: Venn diagram showing tissue-shared TFs in fetal and adult pig macrophages. F: Heatmap showing expression patterns of 51 tissue-specific TFs across 19 tissues in fetal pig macrophages. G: Representative immunofluorescence staining images of DAPI, CD163, and NR4A3 in the tonsil. H: Representative immunofluorescence staining images of DAPI, CD163, and GLMP in the amniotic membrane.

Figure S15D). To finely resolve changes in immune activity between fetal and adult macrophages, we scored macrophages from each matched fetal–adult tissue pair against a panel of 32 immune pathways (Supplementary Table S4). Although minor variability was observed, with fetal scores exceeding adult scores in a small subset of tissues, aggregation of all matched pairs revealed that adult macrophages exhibited significantly higher pathway enrichment scores than fetal macrophages across all examined immune pathways (Supplementary Figure S16A). Collectively, these results suggest that adult macrophages globally possess enhanced immune activity relative to their fetal counterparts.

To systematically dissect the transcriptional regulation of macrophages across fetal and adult stages, we next focused on characterizing TFs that are shared across tissues or specific to particular tissues at each stage. We first identified tissue-shared TFs based on the criteria of being expressed in more than 5% of cells within individual tissues and detected across over 80% of all tissues in this study at the fetal and adult stages, respectively. This criterion ensures we capture TFs with broad functional relevance across most tissues at a given stage. We identified 115 and 113 tissue-shared TFs in fetal and adult stages, respectively, with 97 TFs overlapping between the two stages (Figure 5E; Supplementary Table S4). These overlapping TFs likely constitute a core regulatory module essential for maintaining the fundamental identity and housekeeping functions of macrophages across tissues and developmental time points. Examples include *SPI1*, *IRF8*, *RUNX1* and *STAT1* (Figure 5E), all of which are critical for macrophage development, polarization, and function, underscoring their non-stage-restricted roles (Begitt et al., 2018; Guilliams & Scott, 2017; Langlais et al., 2016; Zhou et al., 2023b).

We then examined tissue-specific TFs in the fetal and adult stages, respectively, defined as those with a Tau value (Yanai et al., 2005) greater than 0.85 (indicating strong enrichment in a single tissue) and expression in more than 5% of macrophages within that tissue. At the fetal stage, we identified 51 tissue-specific TFs distributed across 19 tissues, whereas in the adult stage, we found a larger repertoire of 78 tissue-specific TFs distributed across 28 tissues (Figure 5F; Supplementary Figure S17A and Table S4). The expanded TF repertoire in adulthood (53% increase) may reflect an adaptation to external environmental exposures and tissue functional complexity demands, in stark contrast to the protective intrauterine environment of fetal development. Among these, 10 TFs were detected as tissue-specific in both fetal and adult stages, with nearly identical expression levels at both stages (Supplementary Figure S17B). For instance, *LTF*, an iron-binding protein crucial for innate immune defense against microbial infections (Wu et al., 2011), was specifically enriched in the bone marrow. Similarly, *SPIC*, essential for RPM development and splenic iron recycling (Alam et al., 2020), maintained splenic specificity, reinforcing its non-stage-restricted contribution to iron homeostasis.

We next validated two fetal tissue-specific TFs via immunofluorescence, including the tonsil macrophage-specific TF *NR4A3* and the amniotic membrane macrophage-specific TF *GLMP* (Figures 5G, H). Notably, *GLMP* has not been previously reported in the amniotic membrane. As a lysosomal membrane protein, *GLMP* is involved in critical cellular functions. Prior studies have shown that *Glmp*-deficient mice spontaneously develop liver fibrosis (Nesset et al., 2016), accompanied by the pathological accumulation of lipofuscin and iron within the storage vacuoles of *Glmp*-deficient KCs (Kong et al., 2014). These findings highlight the essential role of *GLMP* in maintaining lysosomal homeostasis and regulating iron metabolism. Collectively, these results delineate a diversity in macrophage transcriptional regulation, where a conserved set of TFs defines macrophage identity and function across stages and tissues, while stage- and tissue-specific TFs mediate local adaptation to distinct microenvironments.

Conservation of fetal macrophages across species

To further explore the cross-species conservation of fetal macrophages, we downloaded single-cell transcriptomic datasets of fetal humans and mice (Fei et al., 2022; Han et al., 2020). Annotated macrophages from organs shared with our atlas were extracted and integrated with the corresponding pig macrophage data from our study. Dimensionality reduction and unsupervised clustering of the integrated dataset identified a total of seven conserved macrophage subtypes (Mφ1–Mφ7) across eight organs (Figure 6A), characterized by the expression of canonical macrophage markers such as *CD68*, *C1QC*, *AIF1*, *IFITM3* and *MRC1* (Figure 6B).

Among these subtypes, Mφ1, Mφ2, and Mφ5 exhibited distinct tissue specificity: Mφ1 was predominantly derived from the liver and highly expressed *TIMD4*, a classic marker for liver-resident KCs (Tran et al., 2020); Mφ2 was enriched in the brain and expressed *P2RY12*, a signature marker of brain-resident MG (Yang et al., 2025); Mφ5 was primarily from the heart and showed functional enrichment in cardiocyte differentiation (Figures 6C, D). Mφ3 was a mouse-dominant subtype with high expression of *S100A6* and *CORO1A*, and was functionally enriched in cell cycle progression and proliferation processes (Figures 6C, D). Mφ4, Mφ6, and Mφ7 were broadly distributed across multiple organs: Mφ4 was defined by high *LYVE1* expression and enrichment in endocytosis; Mφ6 highly expressed *CXCL2* and *NFKBIA*, with enrichment in the response to tumor necrosis factor (Figures 6C, D).

Hierarchical clustering based on gene expression correlations revealed that cells from the same subtype largely grouped together across all species, indicating strong transcriptional conservation (Figure 6E). Notably, for most subtypes, pig and human macrophages clustered closer to each other than to mouse macrophages (Figure 6E). Furthermore, MetaNeighbor analysis (Crow et al., 2018) confirmed significant cross-species transcriptional congruence for all subtypes, with particularly high similarity scores (AUROC>0.8) observed for Mφ3, Mφ4, and Mφ6 (Figure 6E). Collectively, these results demonstrate a remarkable level of transcriptomic evolutionary conservation in fetal macrophages across humans, pigs, and mice.

Functional remodeling and context-specific intercellular interactions of chorioallantoic membrane HBCs in fetal growth restriction

Based on the fetal pig cross-tissue macrophage homeostasis atlas, we sought to investigate the role of macrophages in FGR, a condition predominantly associated with placental insufficiency (Song et al., 2024). HBCs are placental-resident fetal macrophages located within the villi, chorioallantoic membrane, and amniotic membrane (Bezemer et al., 2024; Tang et al., 2011), where they contribute to fetal nutrient

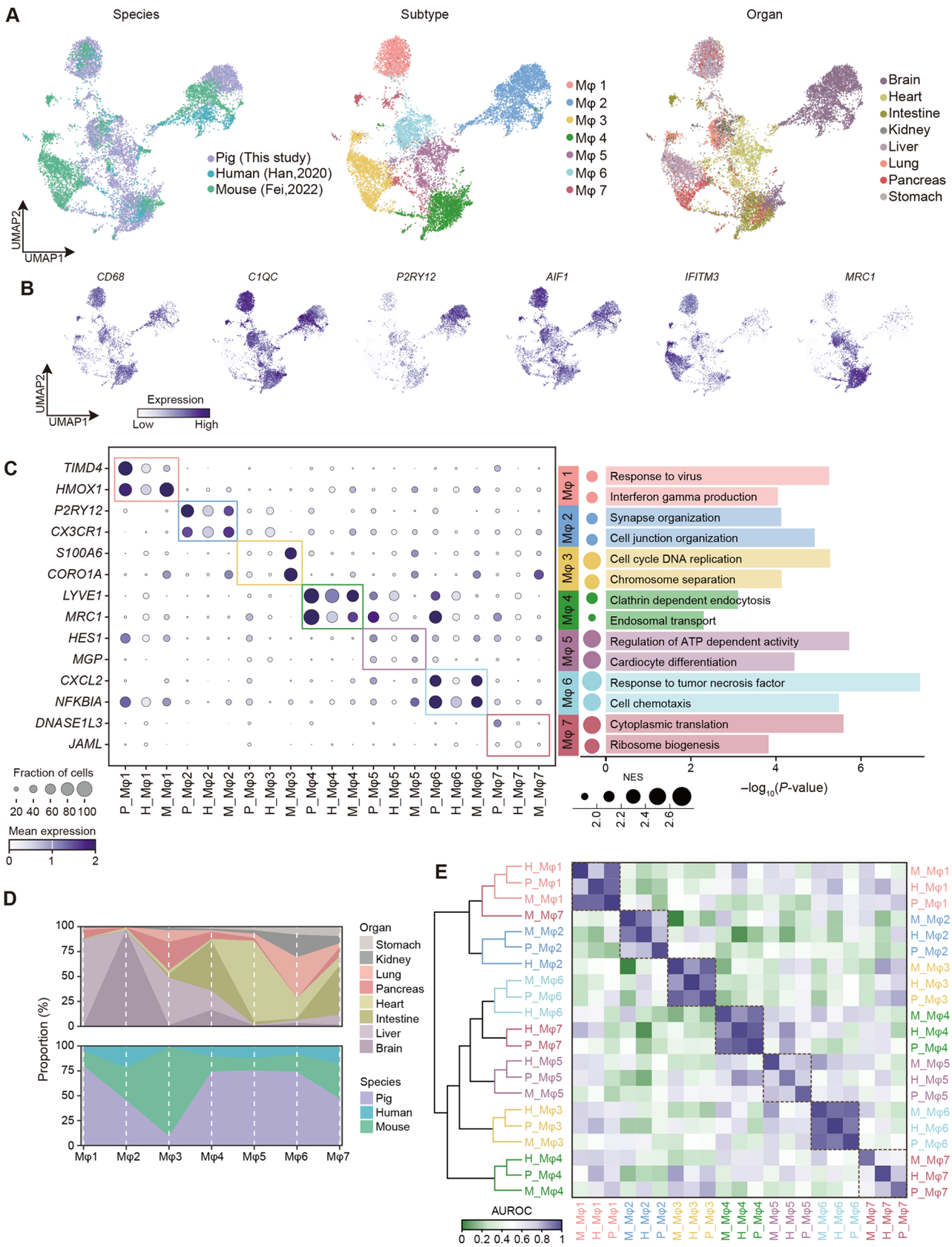


Figure 6 Cross-species comparison of fetal macrophages

A: UMAP visualization of the integrated fetal macrophage atlas from pig, human, and mouse. B: UMAP visualization showing the expression of six macrophage marker genes in the integrated atlas. C: Dot plot showing the expression of selected signature genes for seven macrophage subtypes across species (right). Bar plot showing the enriched GO terms for the seven subtypes (left). D: Area plots showing the tissue origin (top) and species origin (bottom) of the seven macrophage subtypes. E: Dendrogram showing the transcriptional similarity among the seven macrophage subtypes across species (left); heatmap showing the pairwise similarity among the seven subtypes across species (right).

supply, immune defense, and placental vascular development (Reyes & Golos, 2018). To this end, we extracted macrophages from our previously established chorioallantoic membrane single-cell atlas (Cai et al., 2026), comprising samples from five NW and five GR fetuses (Figure 7A; Supplementary Table S5) and across 10 major cell types (Supplementary Figures S18A, B). These extracted macrophages expressed canonical HBC markers (Figure 7B), and integration with our cross-tissue macrophage atlas revealed that they exhibited the highest transcriptional similarity to the HBC PEG10+ subtype identified in the atlas (Supplementary Figures S19A–C). Consequently, we annotated these macrophages as HBCs and further dissected their cellular heterogeneity and transcriptional alterations between GR and NW conditions.

Differential gene expression analysis of HBCs between GR and NW groups revealed a marked upregulation of pro-inflammatory transcriptional signatures in GR. These included canonical inflammatory mediators such as *CCL4*, *CCL8*, *CXCL2*, *TNF*, *TLR5*, *IL18* and *IL1A*, as well as genes involved in the NF-κB signaling pathway (*RELB*, *IKBKG*, *NFKBIA*, *NFKBID* and *NFKBIZ*) (Figure 7C; Supplementary Table S5) (Ping et al., 2019). Additionally, genes associated with hypoxia response (*LDHA*, NDRG1 and *HIF1A*) (Lee et al., 2015) and vascular regulation (*EDN1* and *VEGFA*) (Apte et al., 2019; Virdis et al., 2015) were also highly upregulated in GR HBCs (Figure 7C; Supplementary Table S5). The upregulation of these genes in GR relative to NW was almost universally observed across littermate-matched pairs (Figure 7D; Supplementary Figure S20A), underscoring the robustness of these changes. Previous studies have reported that elevated expression of proinflammatory cytokine TNFα (Cotechini et al., 2014) and the hypoxia-responsive factor HIF-1α (Robb et al., 2017) in FGR placentas, as well as ET-1 (encoded by *EDN1*)-mediated vasoconstriction, are key contributors to FGR (Nishiyama et al., 2017). In contrast, fewer genes were specifically upregulated in NW HBCs, which included genes involved in ion transport (*SLC9A9*), cAMP hydrolysis (*PDE4D*), and histone deacetylation (*HDAC9*) (Figure 7C; Supplementary Table S5). Functional enrichment of DEGs between GR and NW HBCs revealed that GR HBCs were enriched for pathways including the nitric oxide (NO) biosynthetic process, response to oxidative stress, cellular response to hypoxia, TNF signaling pathway, and NF-κB signaling pathway (Figure 7C). These findings indicate that FGR-associated HBCs may integrate inflammatory, hypoxic, and oxidative stress responses to drive vascular dysfunction in FGR (Almasry et al., 2012; Bezemer et al., 2024; Cotechini et al., 2014; Krause et al., 2011; Robb et al., 2017).

To characterize how the intercellular communication networks of HBCs shift in FGR, we performed cell-cell communication analysis using CellChat (Supplementary Table S5) (Jin et al., 2021). Our analysis revealed both conserved and condition-specific signaling pathways shaped by microenvironmental dynamics. When HBCs served as signaling senders (Figure 7E), several interactions were consistently observed in both NW and GR conditions, suggesting the existence of functionally conserved communication axes critical for immune regulation and tissue stability. For instance, HBCs utilized MK and SPP1 signaling pathways to interact with a broad range of cell types except trophoblasts and erythrocytes. Additionally, HBCs communicated with DCs via CCL interactions, including CCL2–CCR2, CCL8–CCR2, CCL8–CCR1, and CCL14–CCR1, which are known to mediate DC adhesion, maturation, and functional activation (Fein et al., 2020). Regarding condition-specific signaling, only the collagen pathway (COL1A2) was uniquely identified in the NW condition. In contrast, under GR conditions, we observed more context-specific interactions. For example, GR HBCs transmitted immune-related signals via the ICAM pathway to DCs and NKT cells (Dalal & Sumagin, 2020), as well as via the TNF pathway to DCs, VECs, and trophoblasts (Arkoudi et al., 2025). They also delivered trophic and remodeling signals through the IGF pathway to trophoblasts (Cedano Prieto et al., 2017) and through the THBS signaling pathway to multiple cell types (Kaur et al., 2021; Lin et al., 2016). Together, these findings indicate that while a conserved core of cellular interactions is maintained, GR HBCs selectively expand the interactome encompassing inflammatory and remodeling signals. Concurrently, GR HBCs lose the NW-specific COL1A2 signaling, which is critical for the composition and structural integrity of the ECM (Ricard-Blum, 2011).

When HBCs acted as signaling receivers (Figure 7F), the conserved signals they received in both NW and GR conditions could be broadly categorized into three major groups. First, immune and inflammatory signaling pathways included IFN-II, TNF, angiopoietin-like protein (ANGPTL), PTPRC, and CCL chemokine axes. Second, cell adhesion signaling comprised VCAM and CADM interactions. Third, growth factor-mediated survival signaling was represented by the CSF pathway. Beyond these conserved networks, GR HBCs engaged in additional interaction pairs not detected in NW HBCs. For instance, immune cells (DCs–, B cells–, T cells–, NKT–) connected to HBCs through the ITGB2 signaling pathway; DCs, SMCs, and fibroblasts used the THBS signaling pathway to communicate with the HBCs; and non-immune cells (SMCs–, trophoblasts–, and fibroblasts–) communicated with HBCs through the MK (MDK–NCL) interaction. Collectively, these results indicate that HBCs regulate their adhesion, survival, and immune states through a shared set of core communication pathways, while GR HBCs acquire unique interactions that may further modulate their behavior.

DISCUSSION

Pigs are not only of major agricultural importance but also represent a critical large animal model for studying complex human diseases, holding promise as potential organ donors given their striking similarities to humans in physiology, anatomy, genetics, metabolism, and organ size (Prather et al., 2013). Single-cell technologies have already advanced our understanding of pig biology across health, disease, evolution, and development (Chen et al., 2025a; Huang & Xiao, 2026; Rao et al., 2023; Xiao et al., 2026; Yao et al., 2025, 2026). In this study, we constructed a comprehensive macrophage single-cell transcriptomic atlas across 54 distinct tissues in healthy late-gestation (peripartum) fetal pigs, representing the most extensive characterization of macrophage heterogeneity during this critical developmental window to date.

In our cross-tissue fetal pig macrophage atlas, we identified two placental anatomical site-specific HBC subtypes, HBC GPNMB+ and HBC PEG10+, predominantly derived from the amniotic membrane and chorioallantoic membrane, respectively. The amniotic membrane serves as a mechanical barrier directly in contact with amniotic fluid, requiring

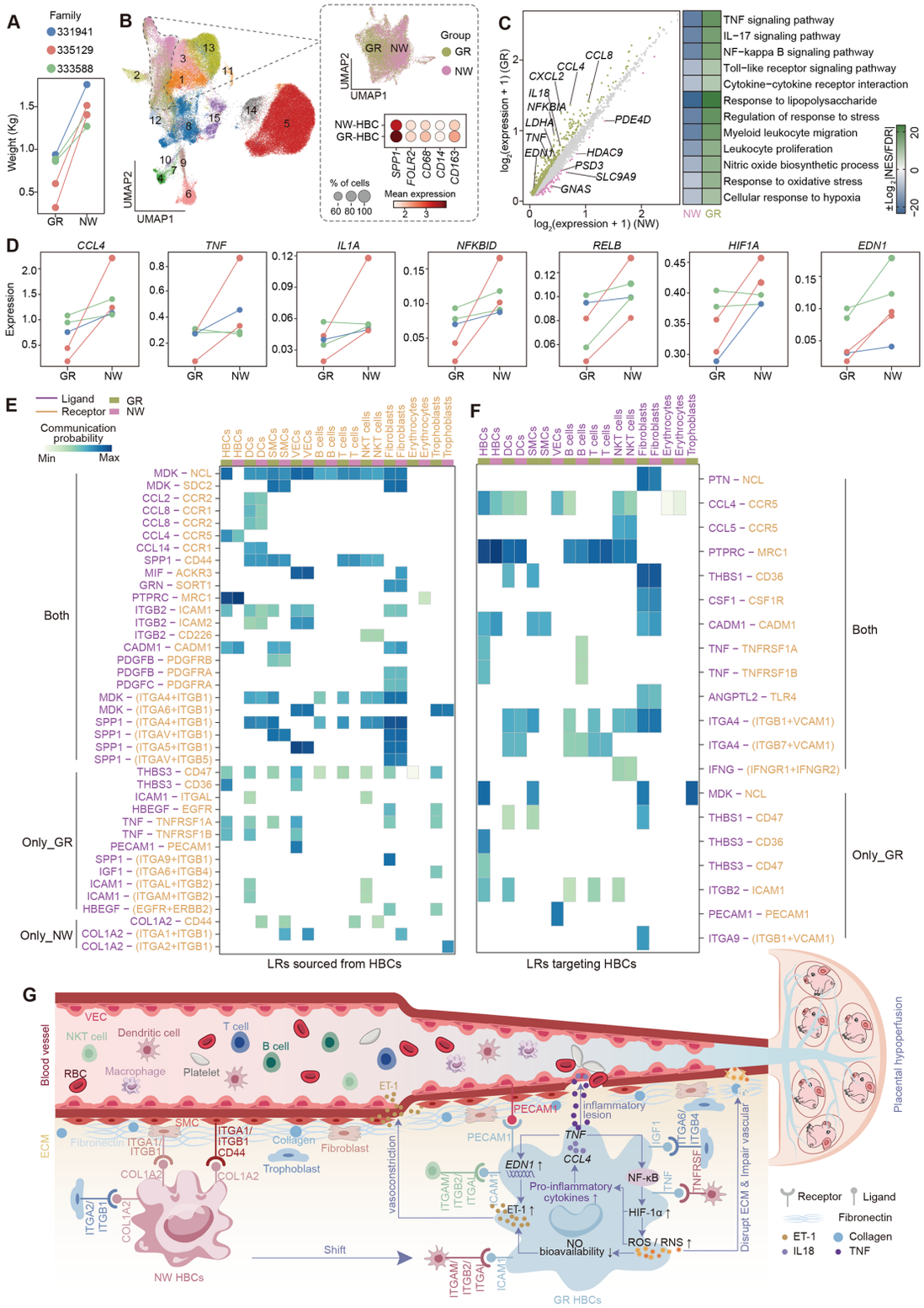


Figure 7 Shift in function and intercellular interactions of chorioallantoic membrane HBCs in FGR

A: Dot plot showing the weights of 10 fetal pigs (5 NW and 5 GR) from 3 litters. B: UMAP visualization showing macrophages from 5 NW and 5 GR fetal pigs integrated with our cross-tissue fetal pig macrophage atlas; numbers and colors in the plot correspond to macrophage subtypes referenced in Figure 1C (left). UMAP showing the macrophages from 5 NW and 5 GR fetal pigs (right top), and dot plot showing the HBC gene markers for NW-HBCs and GR-HBCs (right bottom). C: Volcano plot showing DEGs between GR HBCs and NW HBCs (with cutoffs set as $|\log_2(\text{fold change})|>0.5$ and $P<0.05$), along with functional pathways enriched from these DEGs using gseKEGG and gseGO. Colors represent $\pm\log_2(|\text{NES}|/\text{FDR})$, where green indicates significantly upregulated pathways and blue indicates downregulated ones (NES: normalized enrichment score; FDR: false discovery rate). D: Dot plots showing the expression levels of selected genes in 5 NW and 5 GR fetal pigs. E, F: Heatmaps showing significant ligand-receptor pairs (LRs) in NW and GR HBCs: (E) LRs sourced from HBCs; (F) LRs targeting HBCs. G: Schematic diagram illustrating potential mechanisms by which chorioallantoic membrane HBCs may contribute to fetal growth restriction.

continuous maintenance of its structural integrity and the capacity for rapid repair in response to potential injuries, which is crucial for normal pregnancy progression (Friel et al., 2017; Mohan et al., 2017). Consistent with this physiological demand, the HBC GPNMB+ subtype highly expresses glycolysis-related genes (*LDHA*, *ENO1*) and ECM regulators (*GPNMB*, *ANXA2*, *COL1A1*), with significant enrichment in wound healing and pyruvate metabolism pathways. These features suggest that HBC GPNMB+ maintains amniotic barrier integrity by regulating ECM synthesis and promoting tissue repair, while its high glycolytic activity rapidly generates ATP to support these processes. *GPNMB*, which is expressed in macrophages and promotes tissue repair, has been reported in multiple tissues (Chen et al., 2025b; Ramadoss et al., 2024; Silva et al., 2018), further supporting the role of the HBC GPNMB+ subtype in maintaining the functional homeostasis of the amniotic barrier. In addition, amniotic fluid oxygen tension is consistently lower than that of maternal blood circulation, forming a unique physiological hypoxic microenvironment in the amniotic cavity (De Munck et al., 2019; Zhang et al., 2011). This hypoxic environment aligns with the upregulated glycolysis observed in HBC GPNMB+, indicating that their metabolic specialization is an adaptive response to the local microenvironment. The chorioallantoic membrane is highly vascularized and functions as the primary interface for maternal–fetal exchange, immune tolerance, and placental angiogenesis (Salih et al., 2022; Yang et al., 2017). The chorioallantoic-specific HBC PEG10+ subtype highly expresses immunomodulators (*A2M*, *CCL24*) and the placental development regulator *PEG10*, with enrichment in the immune response activation pathway. Since *A2M* inhibits inflammatory cytokine production (Rehman et al., 2013; Vandooren & Itoh, 2021) and *PEG10* is essential for trophoblast proliferation (Chen et al., 2015) and maintenance of placental vascular architecture (Shiura et al., 2021), we propose that HBC PEG10+ ensures efficient maternal–fetal exchange and normal fetal growth by orchestrating immune regulation and vascular development support. Collectively, these two HBC subtypes may represent specialized adaptations to the distinct functional demands of different placental components. Future studies employing spatial transcriptomics and in vitro functional assays are warranted to precisely localize and validate these functions.

In our study, we identified a robust dichotomy of LYVE1^{high}MHCII^{low} and LYVE1^{low}MHCII^{high} macrophage subtypes across 27 fetal pig tissues, whose transcriptional signatures and putative functions parallel those described in human and mouse (Chakarov et al., 2019; Drieu et al., 2022; Lim et al., 2018; Lund et al., 2024). The LYVE1^{high}MHCII^{low} subtype highly expressed genes involved in endocytosis and vascular interaction (*CD163*, *MRC1*, *CD209*, *COLEC12*, *F13A1*, *SELENOP*) (Supplementary Table S2), mirroring the transcriptional hallmarks of LYVE1+ perivascular macrophages described in mouse and human tissues (Chakarov et al., 2019; Lund et al., 2024). The dependency of this lineage on the TF *Maf*, as established by Moura Silva et al. (2021), is further supported by our findings, suggesting that this genetic program is initiated early and is essential for their identity. Conversely, the LYVE1^{low}MHCII^{high} subtype was enriched in genes associated with antigen presentation (*SLA-DQB1*, *SLA-DRA*, *SLA-DRB1*) and chemokines (*CCL4*, *CCL5*, *CXCL8*) (Supplementary Table S2), consistent with an immune-interacting identity (Chakarov et al., 2019). Their coexistence suggests complementary roles in tissue immunity and homeostasis: LYVE1^{high}MHCII^{low} macrophages serve as sentinels at vascular interfaces, while LYVE1^{low}MHCII^{high} macrophages may more actively engage in immune coordination and inflammatory regulation. As our work reveals that this paradigm is not only conserved across tissues but also across species, this finding highlights a fundamental organizational principle of the macrophage ecosystem under normal physiological conditions.

Our study characterized the conserved and tissue-adapted metabolic programs of fetal macrophages across diverse tissues and revealed their close integration with functional specialization. The TCA cycle and mitochondrial electron transport chain (ETC)-driven OXPHOS form a central axis of cellular energy metabolism, as most cells depend on OXPHOS for efficient ATP production (Liu et al., 2025). We identified a set of core metabolic genes involved in OXPHOS, ROS metabolism, and the TCA cycle that were consistently expressed across diverse tissues, underscoring mitochondrial respiration as a fundamental requirement for macrophages during development (Nolfi-Donegan et al., 2020). A recent study in mouse and human macrophages across ten organs has revealed that macrophages require and differentially use OXPHOS to sustain their identity and function in the steady state (Wculek et al., 2023). Mitochondrial metabolism is increasingly recognized as a key determinant that integrates cellular demands and extracellular cues to regulate macrophage activation states and effector functions (Wang et al., 2021). Beyond this conserved foundation, we further uncovered that macrophages displayed tissue-specific metabolic signatures, which are strongly supported by mounting evidence showing that resident macrophages in different tissues exhibit distinct metabolic profiles tailored to local availability of nutrients and functional demands (Wculek et al., 2024). For instance, similar to our findings in fetal liver macrophages, KCs are known to possess a robust capacity for iron and lipid handling (Blériot et al., 2021; Scott & Guilliams, 2018; Wculek et al., 2024). Our data suggest that the metabolic programming underlying such specialization is established prenatally. Importantly, our correlation analysis highlights that macrophage metabolism and function are tightly coupled, with lysosomal activity emerging as a central coordinator of this relationship. The strong association between lysosomal function and metabolic pathways, most prominently iron and lipid metabolism, reinforces the established role of lysosomes in iron homeostasis and lipid handling in macrophages (Melo & Dvorak, 2012; Rizzollo et al., 2021). While these analyses provide important insights, it is important to acknowledge that our study infers metabolic states from transcriptomic data. Given the inherent limitations of mRNA-based assessments, including temporal discordance between transcript abundance and protein levels, as well as the complex regulation of enzyme activity, our findings should be interpreted as reflecting transcriptional potential rather than direct metabolic fluxes. Thus, future investigations integrating metabolomic and proteomic approaches, combined with functional metabolic flux analyses, are warranted to directly measure metabolic activities underlying the tissue-specific functional specialization of fetal macrophages. In summary, these findings provide additional prenatal evidence that macrophage metabolism is not merely a source of energy and biosynthetic substrates, but a fundamental regulatory axis that shapes macrophage identity and effector programs across

tissue environments.

While sexual dimorphism is commonly observed in the mammalian immune system (Oertelt-Prigione, 2012), our study revealed a high degree of transcriptional similarity between male and female fetal macrophages across multiple tissues. We hypothesize that this observation may be attributed to two key factors: the unique developmental stage and environmental context. First, our samples were derived from male and female fetuses within the same intrauterine environment during late gestation, where sex hormone levels remain low during this period (Bizzarri & Cappa, 2020; Renault et al., 2020). As critical regulators of immune sexual dimorphism (Taneja, 2018), the low abundance of these hormones may prevent the full manifestation of sex-specific phenotypes in macrophages. Second, compared to the complex and variable postnatal environment, the intrauterine environment is relatively mild. Environmental exposures are known to be critical drivers of sex-biased immune responses (Pollard, 2012), as exemplified by the finding of Gal-Oz et al. (2019) that interferon stimulation amplifies sexual dimorphism in macrophages. Future studies should expand the range of tissues analyzed, increase the number of individuals, and incorporate multiple developmental stages to further explore potential sexual differences in macrophages and their underlying regulatory mechanisms.

Focusing on the HBCs in the chorioallantoic membranes of GR and NW fetuses, we found that these HBCs undergo complex functional reprogramming, accompanied by selective remodeling of intercellular communication networks. Specifically, differential gene expression and functional enrichment analyses revealed that GR HBCs amplified classical pro-inflammatory signaling, hypoxia-responsive signatures, NO biosynthetic process, and vasoconstriction regulation (e.g., *CCL4*, *IL1A*, *NFKBID*, *TNF*, *HIF1A* and *EDN1*). Additionally, intercellular interaction analysis showed that whether acting as signal “senders” or “receivers”, GR HBCs displayed more ligand–receptor pairs than NW HBCs (Supplementary Figure S21A), indicating enhanced intercellular communication activity, such as remodeling their interactome to transmit additional inflammatory (e.g., TNF–TNFRSF1A/B) and angiogenic (e.g., HBEGF–EGFR/ERBB2) signals. Prior studies on FGR in human and animal models have observed inflammatory activation, hypoxia signaling, dysregulated NO levels, disrupted ECM, and aberrant vascular regulation in the placenta (Almasry et al., 2012; Cotechini et al., 2014; Dodson et al., 2013; Krause et al., 2011; Kulandavelu et al., 2013; Robb et al., 2017). Our findings in HBCs from FGR pigs align with these observations, thus allowing us to propose a mechanism orchestrated by GR HBCs via a cascade of interactions for FGR (Figure 7G): I) Inflammatory vasoconstriction: GR HBCs overexpress pro-inflammatory cytokines, which induce vasoconstrictor ET-1 production and release. The secreted ET-1 acts on SMCs and VECs, causing sustained vasoconstriction (Nishiyama et al., 2017; Virdis et al., 2015). II) Hypoxia-amplified inflammation: pro-inflammatory cytokines simultaneously promote the accumulation of HIF-1α via NF-κB activation, forming a feed-forward loop where hypoxia further amplifies the inflammatory response while generating damaging ROS/RNS that directly impair vascular structures (Tafani et al., 2016; Tejero et al., 2019; Wang et al., 2013). III) NO dysregulation: The resulting nitrosative stress reduces intracellular NO bioavailability, eliminating its physiological suppression of ET-1 production and thereby exacerbating vasoconstriction (Luo et al., 2016). IV) Endothelial dysfunction: The pro-inflammatory cytokines upregulated in GR HBCs directly act on the vascular endothelium, inducing its contraction and widening intercellular gaps to increase vascular permeability (Kreuger & Phillipson, 2016). V) Collagen signaling loss: Loss of the collagen signaling network, which is essential for establishing immune tolerance at the maternal–fetal interface and maintaining placental barrier integrity, contributes to increased vascular stiffness (Dodson et al., 2013; Shi et al., 2020). Collectively, these mechanisms may converge to disrupt vascular structure and function via sustained vasoconstriction, oxidative/nitrosative damage, impaired vasodilatory capacity, increased vascular permeability, and elevated stiffness. Consequently, uteroplacental perfusion becomes insufficient, leading to limited placental blood flow and reduced nutrient and oxygen delivery to the fetus, ultimately contributing to FGR. Notably, the regulatory pathway of chorioallantoic membrane HBCs in FGR proposed herein is solely based on single-cell transcriptomic data; thus, further validation at the protein and functional levels is required. For example, chorioallantoic membrane HBCs from NW fetuses could be cultured under normoxic, hypoxic, and hypoxic+HIF-1α inhibitor conditions. Western blot and ELISA assays can then be used to detect the expression and secretion of inflammatory factors (e.g., TNF, IL1A) and HIF-1α, thereby validating the regulatory role of the hypoxia–inflammation response in HBCs under simulated hypoxic microenvironments. Furthermore, co-culturing HBCs from NW and GR fetuses with placental fibroblasts could elucidate their differential impact on the ECM; quantitative measurement of COL1A2 secretion and collagen fiber density can detect whether GR HBCs induce more loss of collagen components. Future studies should also explore the contribution of other cell types (e.g., trophoblasts, VECs) to FGR pathology through multi-omics analyses, as HBC-mediated mechanisms do not operate in isolation. Additionally, expanding the range of tissue samples included in such investigations will further enhance the comprehensiveness of these findings.

DATA AVAILABILITY

The raw sequencing data were derived from our previous study (Cai et al., 2026) and are deposited in the Genome Sequence Archive (GSA) under accession number CRA010159. The processed gene expression matrices generated in this work are available in the Science Data Bank (DOI: 10.57760/sciencedb.j00139.00279), and analysis codes generated for this study are available on Figshare (DOI: 10.6084/m9.figshare.31568644).

SUPPLEMENTARY DATA

Supplementary data to this article can be found online.

COMPETING INTERESTS

The authors declare that they have no competing interests.

AUTHORS’ CONTRIBUTIONS

L.P.C. and L.C.L. conceptualized and designed the study and supervised the project. L.C.L. and X.Y.C. performed data quality control and analysis; L.C.L. drafted the original manuscript and conducted experimental validation. L.P.C. and X.Y.C. critically reviewed and revised the manuscript. All authors read and approved the final version of the manuscript.

ACKNOWLEDGMENTS

We gratefully acknowledge all members of the National Key Laboratory for Swine Genetic Improvement and Germplasm Innovation for their contributions to sample collection and data curation.

REFERENCES

Ahl PJ, Hopkins RA, Xiang WW, et al. 2020. Met-flow, a strategy for single-cell metabolic analysis highlights dynamic changes in immune subpopulations. *Communications Biology*, **3**(1): 305.

Alam Z, Devalaraja S, Li MH, et al. 2020. Counter regulation of *Spic* by NF-κB and STAT signaling controls inflammation and iron metabolism in macrophages. *Cell Reports*, **31**(13): 107825.

Almasry SM, Eldomiaty MA, Elfayomy AK, et al. 2012. Expression pattern of tumor necrosis factor alpha in placentae of idiopathic fetal growth restriction. *Journal of Molecular Histology*, **43**(3): 253–261.

Ander SE, Diamond MS, Coyne CB. 2019. Immune responses at the maternal-fetal interface. *Science Immunology*, **4**(31): eaat6114.

Apte RS, Chen DS, Ferrara N. 2019. VEGF in signaling and disease: beyond discovery and development. *Cell*, **176**(6): 1248–1264.

Arkoudi K, Yuan Y, Cumine AP, et al. 2025. An NF-kB/TNF-alpha signalling feedback loop acts to coordinate tissue regeneration and macrophage behaviour in zebrafish. *npj Regenerative Medicine*, **10**(1): 27.

Artyomov MN, Van Den Bossche J. 2020. Immunometabolism in the single-cell era. *Cell Metabolism*, **32**(5): 710–725.

Begitt A, Cavey J, Droescher M, et al. 2018. On the role of *STAT1* and *STAT6* ADP-ribosylation in the regulation of macrophage activation. *Nature Communications*, **9**(1): 2144.

Berezhna VA, Mamontova TV, Gromova AM. 2021. Cd68+ M1 macrophages is associated with placental insufficiency under fetal growth restriction. *Wiadomości Lekarskie*, **74**(2): 213–219.

Bezemer RE, Faas MM, Van Goor H, et al. 2024. Decidual macrophages and Hofbauer cells in fetal growth restriction. *Frontiers in Immunology*, **15**: 1379537.

Bezemer RE, Schoots MH, Timmer A, et al. 2020. Altered levels of decidual immune cell subsets in fetal growth restriction, stillbirth, and placental pathology. *Frontiers in Immunology*, **11**: 1898.

Bizzarri C, Cappa M. 2020. Ontogeny of hypothalamus-pituitary gonadal axis and minipuberty: an ongoing debate?. *Frontiers in Endocrinology*, **11**: 187.

Blériot C, Barreby E, Dunsmore G, et al. 2021. A subset of Kupffer cells regulates metabolism through the expression of *CD36*. *Immunity*, **54**(9): 2101–2116. e6.

Blériot C, Chakarov S, Ginhoux F. 2020. Determinants of resident tissue macrophage identity and function. *Immunity*, **52**(6): 957–970.

Bogie JFJ, Grajchen E, Wouters E, et al. 2020. Stearoyl-CoA desaturase-1 impairs the reparative properties of macrophages and microglia in the brain. *Journal of Experimental Medicine*, **217**(5): e20191660.

Buck MD, O'Sullivan D, Pearce EL. 2015. T cell metabolism drives immunity. *Journal of Experimental Medicine*, **212**(9): 1345–1360.

Cai LP, Zhang Q, Yao TX, et al. 2026. Family single-cell atlases reveal pig pregnancy and fetal growth restriction critical cell types. *Science*, **391**(6792): eadu7265.

Cedano Prieto DM, Cheng YS, Chang CC, et al. 2017. Direct integrin binding to insulin-like growth factor-2 through the C-domain is required for insulin-like growth factor receptor type 1 (IGF1R) signaling. *PLoS One*, **12**(9): e0184285.

Chakarov S, Lim HY, Tan L, et al. 2019. Two distinct interstitial macrophage populations coexist across tissues in specific subtissular niches. *Science*, **363**(6432): eaau0964.

Chen GB, Tan CS, Teh BK, et al. 2011. Molecular mechanisms for synchronized transcription of three complement C1q subunit genes in dendritic cells and macrophages. *Journal of Biological Chemistry*, **286**(40): 34941–34950.

Chen HY, Sun MN, Liu J, et al. 2015. Silencing of paternally expressed gene 10 inhibits trophoblast proliferation and invasion. *PLoS One*, **10**(12): e0144845.

Chen XY, Lai CL, Cai LP, et al. 2025a. Cross one single body 49 tissues single-cell transcriptome reveals detailed macrophage heterogeneity during pig pregnancy. *Frontiers in Immunology*, **16**: 1574120.

Chen YF, Lee CW, Li YSJ, et al. 2025b. Temporal single-cell sequencing analysis reveals that *GPNMB*-expressing macrophages potentiate muscle regeneration. *Experimental & Molecular Medicine*, **57**(6): 1232–1245.

Chu A, Najafzadeh P, Sullivan P, et al. 2019. Aldehyde dehydrogenase isoforms and inflammatory cell populations are differentially expressed in term human placentas affected by intrauterine growth restriction. *Placenta*, **81**: 9–17.

Cortal A, Martignetti L, Six E, et al. 2021. Gene signature extraction and cell identity recognition at the single-cell level with Cell-ID. *Nature Biotechnology*, **39**(9): 1095–1102.

Cotechini T, Komisarenko M, Sperou A, et al. 2014. Inflammation in rat pregnancy inhibits spiral artery remodeling leading to fetal growth restriction and features of preeclampsia. *Journal of Experimental Medicine*, **211**(1): 165–179.

Crow M, Paul A, Ballouz S, et al. 2018. Characterizing the replicability of cell types defined by single cell RNA-sequencing data using MetaNeighbor. *Nature Communications*, **9**(1): 884.

Dalal PJ, Sumagin R. 2020. Emerging functions of ICAM-1 in macrophage efferocytosis and wound healing. *Journal of Cellular Immunology*, **2**(5): 250–253.

Davies LC, Rice CM, Palmieri EM, et al. 2017. Peritoneal tissue-resident macrophages are metabolically poised to engage microbes using tissue-niche fuels. *Nature Communications*, **8**(1): 2074.

De Munck N, Janssens R, Segers I, et al. 2019. Influence of ultra-low oxygen (2%) tension on *in-vitro* human embryo development. *Human Reproduction*, **34**(2): 228–234.

Deng ZH, Loyher PL, Lazarov T, et al. 2024. The nuclear factor *ID3* endows macrophages with a potent anti-tumour activity. *Nature*, **626**(8000): 864–873.

Dick SA, Wong A, Hamidzada H, et al. 2022. Three tissue resident macrophage subsets coexist across organs with conserved origins and life cycles. *Science Immunology*, **7**(67): eabf7777.

Dodson RB, Rozance PJ, Fleenor BS, et al. 2013. Increased arterial stiffness and extracellular matrix reorganization in intrauterine growth–restricted fetal sheep. *Pediatric Research*, **73**(2): 147–154.

Domanska D, Majid U, Karlsen VT, et al. 2022. Single-cell transcriptomic analysis of human colonic macrophages reveals niche-specific subsets. *Journal of Experimental Medicine*, **219**(3): e20211846.

Domínguez Conde C, Xu C, Jarvis LB, et al. 2022. Cross-tissue immune cell analysis reveals tissue-specific features in humans. *Science*, **376**(6594): eabl5197.

Drieu A, Du SL, Storck SE, et al. 2022. Parenchymal border macrophages regulate the flow dynamics of the cerebrospinal fluid. *Nature*, **611**(7936): 585–593.

Eraslan G, Drokhlyansky E, Anand S, et al. 2022. Single-nucleus cross-tissue molecular reference maps toward understanding disease gene function. *Science*, **376**(6594): eabl4290.

Fei LJ, Chen HD, Ma LF, et al. 2022. Systematic identification of cell-fate regulatory programs using a single-cell atlas of mouse development. *Nature Genetics*, **54**(7): 1051–1061.

Fein MR, He XY, Almeida AS, et al. 2020. Cancer cell *CCR2* orchestrates suppression of the adaptive immune response. *Journal of Experimental Medicine*, **217**(10): e20181551.

Figueras F, Caradeux J, Crispi F, et al. 2018. Diagnosis and surveillance of late-onset fetal growth restriction. *American Journal of Obstetrics and Gynecology*, **218**(2): S790–S802. e1.

Franzén O, Gan LM, Björkegren JLM. 2019. PanglaoDB: a web server for exploration of mouse and human single-cell RNA sequencing data.

Database, **2019**(1): baz046.
Frenis K, Badalamenti B, Mamigonian O, et al. 2025. Path of differentiation defines human macrophage identity. *BioRxiv*, https://doi.org/10.1101/2025.01.24.634694.
Friel NA, De Girolamo L, Gomoll AH, et al. 2017. Amniotic fluid, cells, and membrane application. *Operative Techniques in Sports Medicine*, **25**(1): 20–24.
Gal-Oz ST, Maier B, Yoshida H, et al. 2019. ImmGen report: sexual dimorphism in the immune system transcriptome. *Nature Communications*, **10**(1): 4295.
Ginhoux F, Guilliams M. 2016. Tissue-resident macrophage ontogeny and homeostasis. *Immunity*, **44**(3): 439–449.
Gordon S, Plüddemann A. 2017. Tissue macrophages: heterogeneity and functions. *BMC Biology*, **15**(1): 53.
Guan F, Wang RX, Yi ZJ, et al. 2025. Tissue macrophages: origin, heterogenity, biological functions, diseases and therapeutic targets. *Signal Transduction and Targeted Therapy*, **10**(1): 93.
Guilliams M, Scott CL. 2017. Does niche competition determine the origin of tissue-resident macrophages?. *Nature Reviews Immunology*, **17**(7): 451–460.
Hamilton LK, Moquin-Beaudry G, Mangahas CL, et al. 2022. Stearoyl-CoA Desaturase inhibition reverses immune, synaptic and cognitive impairments in an Alzheimer's disease mouse model. *Nature Communications*, **13**(1): 2061.
Han XP, Zhou ZM, Fei LJ, et al. 2020. Construction of a human cell landscape at single-cell level. *Nature*, **581**(7808): 303–309.
Hao YH, Hao S, Andersen-Nissen E, et al. 2021. Integrated analysis of multimodal single-cell data. *Cell*, **184**(13): 3573–3587. e29.
Harrison PW, Amode MR, Austine-Orimoloye O, et al. 2024. Ensembl 2024. *Nucleic Acids Research*, **52**(D1): D891–D899.
Hartmann FJ, Mrdjen D, Mccaffrey E, et al. 2021. Single-cell metabolic profiling of human cytotoxic T cells. *Nature Biotechnology*, **39**(2): 186–197.
Heieis GA, Patente TA, Almeida L, et al. 2023. Metabolic heterogeneity of tissue-resident macrophages in homeostasis and during helminth infection. *Nature Communications*, **14**(1): 5627.
Hie B, Bryson B, Berger B. 2019. Efficient integration of heterogeneous single-cell transcriptomes using Scanorama. *Nature Biotechnology*, **37**(6): 685–691.
Holtman IR, Skola D, Glass CK. 2017. Transcriptional control of microglia phenotypes in health and disease. *The Journal of Clinical Investigation*, **127**(9): 3220–3229.
Huang F, Xiao YY. 2026. Dynamic lung single-cell atlas of domesticated and wild pigs. *Science China Life Sciences*, **69**(6): 2119–2122.
Jenne CN, Kubes P. 2013. Immune surveillance by the liver. *Nature Immunology*, **14**(10): 996–1006.
Jin SQ, Guerrero-Juarez CF, Zhang LH, et al. 2021. Inference and analysis of cell-cell communication using CellChat. *Nature Communications*, **12**(1): 1088.
Kaminow B, Yunusov D, Dobin A. 2021. STARsolo: accurate, fast and versatile mapping/quantification of single-cell and single-nucleus RNA-seq data. *BioRxiv*, https://doi.org/10.1101/2021.05.05.442755.
Kaur S, Isenberg JS, Roberts DD. 2021. CD47 (cluster of differentiation 47). *Atlas of Genetics and Cytogenetics in Oncology and Haematology*, **25**(2): 83–102.
Kong XY, Nesset CK, Damme M, et al. 2014. Loss of lysosomal membrane protein NCU-G1 in mice results in spontaneous liver fibrosis with accumulation of lipofuscin and iron in Kupffer cells. *Disease Models & Mechanisms*, **7**(3): 351–362.
Korsunsky I, Millard N, Fan J, et al. 2019. Fast, sensitive and accurate integration of single-cell data with Harmony. *Nature Methods*, **16**(12): 1289–1296.
Krause BJ, Hanson MA, Casanello P. 2011. Role of nitric oxide in placental vascular development and function. *Placenta*, **32**(11): 797–805.
Kreuger J, Phillipson M. 2016. Targeting vascular and leukocyte communication in angiogenesis, inflammation and fibrosis. *Nature Reviews Drug Discovery*, **15**(2): 125–142.
Kulandavelu S, Whiteley KJ, Bainbridge SA, et al. 2013. Endothelial NO synthase augments fetoplacental blood flow, placental vascularization, and fetal growth in mice. *Hypertension*, **61**(1): 259–266.
Langlais D, Barreiro LB, Gros P. 2016. The macrophage IRF8/IRF1 regulome is required for protection against infections and is associated with chronic inflammation. *Journal of Experimental Medicine*, **213**(4): 585–603.
Lavin Y, Mortha A, Rahman A, et al. 2015. Regulation of macrophage development and function in peripheral tissues. *Nature Reviews Immunology*, **15**(12): 731–744.
Lazarov T, Juarez-Carreño S, Cox N, et al. 2023. Physiology and diseases of tissue-resident macrophages. *Nature*, **618**(7966): 698–707.
Lee DC, Sohn HA, Park ZY, et al. 2015. A lactate-induced response to hypoxia. *Cell*, **161**(3): 595–609.
Li QY, Barres BA. 2018. Microglia and macrophages in brain homeostasis and disease. *Nature Reviews Immunology*, **18**(4): 225–242.
Li SS, Yu JL, Huber A, et al. 2022. Metabolism drives macrophage heterogeneity in the tumor microenvironment. *Cell Reports*, **39**(1): 110609.
Li Y, Zhang H, Su WP, et al. 2018. Effects of dietary *Bacillus amyloliquefaciens* supplementation on growth performance, intestinal morphology, inflammatory response, and microbiota of intra-uterine growth retarded weanling piglets. *Journal of Animal Science and Biotechnology*, **9**(1): 22.
Lim HY, Lim SY, Tan CK, et al. 2018. Hyaluronan receptor *LYVE-1*-expressing macrophages maintain arterial tone through hyaluronan-mediated regulation of smooth muscle cell collagen. *Immunity*, **49**(2): 326–341. e7.
Lin D, Chun TH, Kang L. 2016. Adipose extracellular matrix remodelling in obesity and insulin resistance. *Biochemical Pharmacology*, **119**: 8–16.
Liu H, Wang S, Wang JH, et al. 2025. Energy metabolism in health and diseases. *Signal Transduction and Targeted Therapy*, **10**(1): 69.
Lund H, Hunt MA, Kurtović Z, et al. 2024. CD163+ macrophages monitor enhanced permeability at the blood–dorsal root ganglion barrier. *Journal of Experimental Medicine*, **221**(2): e20230675.
Luo KH, Thaete LG, Neerhof MG. 2016. Endothelin receptor a antagonism and fetal growth in endothelial nitric oxide synthase gene knockout maternal and fetal mice. *Reproductive Sciences*, **23**(8): 1028–1036.
Mass E, Ballesteros I, Farlik M, et al. 2016. Specification of tissue-resident macrophages during organogenesis. *Science*, **353**(6304): aaf4238.
Melo RCN, Dvorak AM. 2012. Lipid body–phagosome interaction in macrophages during infectious diseases: host defense or pathogen survival strategy?. *PLoS Pathogens*, **8**(7): e1002729.
Miller SL, Huppi PS, Mallard C. 2016. The consequences of fetal growth restriction on brain structure and neurodevelopmental outcome. *The Journal of Physiology*, **594**(4): 807–823.
Miyamoto Y, Kikuta J, Matsui T, et al. 2024. Periportal macrophages protect against commensal-driven liver inflammation. *Nature*, **629**(8013): 901–909.
Mohan R, Bajaj A, Gundappa M. 2017. Human amnion membrane: potential applications in oral and periodontal field. *Journal of International Society of Preventive and Community Dentistry*, **7**(1): 15–21.
Moura Silva H, Kitoko JZ, Queiroz CP, et al. 2021. c-MAF–dependent perivascular macrophages regulate diet-induced metabolic syndrome. *Science Immunology*, **6**(64): eabg7506.
Nesset CK, Kong XY, Damme M, et al. 2016. Age-dependent development of liver fibrosis in *Glmp* $^{gt/gt}$ mice. *Fibrogenesis & Tissue Repair*, **9**(1): 5.
Nishiyama SK, Zhao J, Wray DW, et al. 2017. Vascular function and endothelin-1: tipping the balance between vasodilation and

vasoconstriction. *Journal of Applied Physiology*, **122**(2): 354–360.
Nobs SP, Kopf M. 2021. Tissue-resident macrophages: guardians of organ homeostasis. *Trends in Immunology*, **42**(6): 495–507.
Nolfi-Donegan D, Braganza A, Shiva S. 2020. Mitochondrial electron transport chain: oxidative phosphorylation, oxidant production, and methods of measurement. *Redox Biology*, **37**: 101674.
Oertelt-Prigione S. 2012. The influence of sex and gender on the immune response. *Autoimmunity Reviews*, **11**(6-7): A479–A485.
Ping Z, Chen S, Hermans SJF, et al. 2019. Activation of NF-κB driven inflammatory programs in mesenchymal elements attenuates hematopoiesis in low-risk myelodysplastic syndromes. *Leukemia*, **33**(2): 536–541.
Polański K, Young MD, Miao ZC, et al. 2020. BBKNN: fast batch alignment of single cell transcriptomes. *Bioinformatics*, **36**(3): 964–965.
Pollard KM. 2012. Gender differences in autoimmunity associated with exposure to environmental factors. *Journal of Autoimmunity*, **38**(2-3): J177–J186.
Prabhudas M, Bonney E, Caron K, et al. 2015. Immune mechanisms at the maternal-fetal interface: perspectives and challenges. *Nature Immunology*, **16**(4): 328–334.
Prather RS, Lorson M, Ross JW, et al. 2013. Genetically engineered pig models for human diseases. *Annual Review of Animal Biosciences*, **1**: 203–219.
Rakina M, Larionova I, Kzhyshkowska J. 2024. Macrophage diversity in human cancers: new insight provided by single-cell resolution and spatial context. *Heliyon*, **10**(7): e28332.
Ramadoss S, Qin J, Tao B, et al. 2024. Bone-marrow macrophage-derived GPNMB protein binds to orphan receptor GPR39 and plays a critical role in cardiac repair. *Nature Cardiovascular Research*, **3**(11): 1356–1373.
Rao L, Cai LP, Huang LS. 2023. Single-cell dynamics of liver development in postnatal pigs. *Science Bulletin*, **68**(21): 2583–2597.
Rehman AA, Ahsan H, Khan FH. 2013. Alpha‐2‐macroglobulin: a physiological guardian. *Journal of Cellular Physiology*, **228**(8): 1665–1675.
Remmerie A, Scott CL. 2018. Macrophages and lipid metabolism. *Cellular Immunology*, **330**: 27–42.
Renault CH, Aksglaede L, Wøjdemann D, et al. 2020. Minipuberty of human infancy–a window of opportunity to evaluate hypogonadism and differences of sex development?. *Annals of Pediatric Endocrinology & Metabolism*, **25**(2): 84–91.
Reyes L, Golos TG. 2018. Hofbauer cells: their role in healthy and complicated pregnancy. *Frontiers in Immunology*, **9**: 2628.
Ricard-Blum S. 2011. The collagen family. *Cold Spring Harbor Perspectives in Biology*, **3**(1): a004978.
Rizzollo F, More S, Vangheluwe P, et al. 2021. The lysosome as a master regulator of iron metabolism. *Trends in Biochemical Sciences*, **46**(12): 960–975.
Robb KP, Cotechini T, Allaire C, et al. 2017. Inflammation-induced fetal growth restriction in rats is associated with increased placental HIF-1α accumulation. *PLoS One*, **12**(4): e0175805.
Saha S, Shalova IN, Biswas SK. 2017. Metabolic regulation of macrophage phenotype and function. *Immunological Reviews*, **280**(1): 102–111.
Salih MM, Ali LE, Eed EM, et al. 2022. Histomorphometric study of placental blood vessels of chorion and chorionic villi vascular area among women with preeclampsia. *Placenta*, **124**: 44–47.
Schulz C, Perdiguero EG, Chorro L, et al. 2012. A lineage of myeloid cells independent of Myb and hematopoietic stem cells. *Science*, **336**(6077): 86–90.
Scott CL, Guilliams M. 2018. The role of Kupffer cells in hepatic iron and lipid metabolism. *Journal of Hepatology*, **69**(5): 1197–1199.
Shi JW, Lai ZZ, Yang HL, et al. 2020. Collagen at the maternal-fetal interface in human pregnancy. *International Journal of Biological Sciences*, **16**(12): 2220–2234.
Shiura H, Ono R, Tachibana S, et al. 2021. *PEG10* viral aspartic protease domain is essential for the maintenance of fetal capillary structure in the mouse placenta. *Development*, **148**(19): dev199564.
Silva WN, Prazeres PHDM, Paiva AE, et al. 2018. Macrophage-derived GPNMB accelerates skin healing. *Experimental Dermatology*, **27**(6): 630–635.
Song WH, Guo Q, Puttabyatappa M, et al. 2024. FGR-associated placental insufficiency and capillary angiogenesis involves disruptions in human placental miRNAs and mRNAs. *Heliyon*, **10**(6): e28007.
Sun YL, Wei KF, Liao XD, et al. 2025. Lipid metabolism in microglia: emerging mechanisms and therapeutic opportunities for neurodegenerative diseases (review). *International Journal of Molecular Medicine*, **56**(3): 139.
Suo CQ, Dann E, Goh I, et al. 2022. Mapping the developing human immune system across organs. *Science*, **376**(6597): eabo0510.
Tafani M, Sansone L, Limana F, et al. 2016. The interplay of reactive oxygen species, hypoxia, inflammation, and sirtuins in cancer initiation and progression. *Oxidative Medicine and Cellular Longevity*, **2016**(1): 3907147.
Taneja V. 2018. Sex hormones determine immune response. *Frontiers in Immunology*, **9**: 1931.
Tang ZH, Abrahams VM, Mor G, et al. 2011. Placental Hofbauer cells and complications of pregnancy. *Annals of the New York Academy of Sciences*, **1221**(1): 103–108.
Tejero J, Shiva S, Gladwin MT. 2019. Sources of vascular nitric oxide and reactive oxygen species and their regulation. *Physiological Reviews*, **99**(1): 311–379.
The UniProt Consortium. 2015. UniProt: a hub for protein information. *Nucleic Acids Research*, **43**(D1): D204–D212.
Thomas JR, Naidu P, Appios A, et al. 2021. The ontogeny and function of placental macrophages. *Frontiers in Immunology*, **12**: 771054.
Tran S, Baba I, Poupel L, et al. 2020. Impaired Kupffer cell self-renewal alters the liver response to lipid overload during non-alcoholic steatohepatitis. *Immunity*, **53**(3): 627–640. e5.
Van De Sande B, Flerin C, Davie K, et al. 2020. A scalable SCENIC workflow for single-cell gene regulatory network analysis. *Nature Protocols*, **15**(7): 2247–2276.
Van Ginneken C, Ayuso M, Van Bockstal L, et al. 2023. Preweaning performance in intrauterine growth-restricted piglets: characteristics and interventions. *Molecular Reproduction and Development*, **90**(7): 697–707.
Vandooren J, Itoh Y. 2021. Alpha-2-macroglobulin in inflammation, immunity and infections. *Frontiers in Immunology*, **12**: 803244.
Virdis A, Duranti E, Rossi C, et al. 2015. Tumour necrosis factor-alpha participates on the endothelin-1/nitric oxide imbalance in small arteries from obese patients: role of perivascular adipose tissue. *European Heart Journal*, **36**(13): 784–794.
Wang P, Qi HB, Sun CH, et al. 2013. Overexpression of hypoxia-inducible factor-1α exacerbates endothelial barrier dysfunction induced by hypoxia. *Cellular Physiology and Biochemistry*, **32**(4): 859–870.
Wang YF, Li N, Zhang X, et al. 2021. Mitochondrial metabolism regulates macrophage biology. *Journal of Biological Chemistry*, **297**(1): 100904.
Wang ZS, Wu ZS, Wang H, et al. 2023. An immune cell atlas reveals the dynamics of human macrophage specification during prenatal development. *Cell*, **186**(20): 4454–4471. e19.
Warr A, Affara N, Aken B, et al. 2020. An improved pig reference genome sequence to enable pig genetics and genomics research. *GigaScience*, **9**(6): giaa051.
Wculek SK, Dunphy G, Heras-Murillo I, et al. 2022. Metabolism of tissue macrophages in homeostasis and pathology. *Cellular & Molecular Immunology*, **19**(3): 384–408.
Wculek SK, Forisch S, Miguel V, et al. 2024. Metabolic homeostasis of tissue macrophages across the lifespan. *Trends in Endocrinology &*

Metabolism, **35**(9): 793–808.
Wculek SK, Heras-Murillo I, Mastrangelo A, et al. 2023. Oxidative phosphorylation selectively orchestrates tissue macrophage homeostasis. *Immunity*, **56**(3): 516–530. e9.
Wolf FA, Angerer P, Theis FJ. 2018. SCANPY: large-scale single-cell gene expression data analysis. *Genome Biology*, **19**(1): 15.
Wu Q, Jiang D, Minor MN, et al. 2011. In vivo function of airway epithelial TLR2 in host defense against bacterial infection. *American Journal of Physiology-Lung Cellular and Molecular Physiology*, **300**(4): L579–L586.
Xiao YY, Zou XX, Yang B, et al. 2026. Single-nucleus transcriptome profiling of wild boar and domestic pig intestines reveals the spatiotemporal dynamics of immunity and nutrient absorption. *Science China Life Sciences*, **69**(2): 579–596.
Xu DM, Huang SK. 2020. *IL-33*: a key player in the development of iron-recycling red pulp macrophages. *Cellular & Molecular Immunology*, **17**(12): 1218–1219.
Yanai I, Benjamin H, Shmoish M, et al. 2005. Genome-wide midrange transcription profiles reveal expression level relationships in human tissue specification. *Bioinformatics*, **21**(5): 650–659.
Yang H, Wu JY, Huang XC, et al. 2022. *ABO* genotype alters the gut microbiota by regulating GalNAc levels in pigs. *Nature*, **606**(7913): 358–367.
Yang HX, Chelariu-Raicu A, Makri D, et al. 2023. Updates of placental macrophages: origins, molecular markers, functions, and related diseases. *Journal of Reproductive Immunology*, **157**: 103942.
Yang SW, Cho EH, Choi SY, et al. 2017. DC-SIGN expression in Hofbauer cells may play an important role in immune tolerance in fetal chorionic villi during the development of preeclampsia. *Journal of Reproductive Immunology*, **124**: 30–37.
Yang SY, Jing QQ, Duan WX, et al. 2025. Microglial function alterations during healthy ageing and canine cognitive dysfunction revealed by single-nucleus and spatial transcriptomics. *National Science Review*, https://doi.org/10.1093/nsr/nwaf388.
Yao TX, Li N, Huang LS. 2025. Integrated single-cell transcriptomic map of pig kidney cells across various periods and anatomical sites. *Zoological Research*, **46**(2): 469–482.
Yao TX, Zhang Y, Chen XY, et al. 2026. Dynamic single-nucleus transcriptomic profiling of kidney development in Bamaxiang and Wild Boar. *Zoological Research*, **47**(1): 58–71.
Yona S, Kim KW, Wolf Y, et al. 2013. Fate mapping reveals origins and dynamics of monocytes and tissue macrophages under homeostasis. *Immunity*, **38**(1): 79–91.
Yu GC, Wang LG, Han YY, et al. 2012. clusterProfiler: an R package for comparing biological themes among gene clusters. *OMICS: A Journal of Integrative Biology*, **16**(5): 284–287.
Zhang K, Zhu LL, Fan M. 2011. Oxygen, a key factor regulating cell behavior during neurogenesis and cerebral diseases. *Frontiers in Molecular Neuroscience*, **4**: 5.
Zheng LT, Qin SS, Si W, et al. 2021. Pan-cancer single-cell landscape of tumor-infiltrating T cells. *Science*, **374**(6574): abe6474.
Zhou QX, Zhao CL, Yang ZY, et al. 2023a. Cross-organ single-cell transcriptome profiling reveals macrophage and dendritic cell heterogeneity in zebrafish. *Cell Reports*, **42**(7): 112793.
Zhou SY, Zhao T, Chen XQ, et al. 2023b. Runx1 deficiency promotes M2 macrophage polarization through enhancing STAT6 phosphorylation. *Inflammation*, **46**(6): 2241–2253.